# Redox-active metal-organic frameworks for the removal of contaminants of emerging concern

Submitted version made available in agreement with publisher's policy.

Please, cite as follows:

Chizoba I. Ezugwu, Jayesh M Sonawane, Roberto Rosal, Redox-active metal-organic frameworks for the removal of contaminants of emerging concern, Separation and Purification Technology, 284, 2022, 120246, https://doi.org/10.1016/j.seppur.2021.120246.

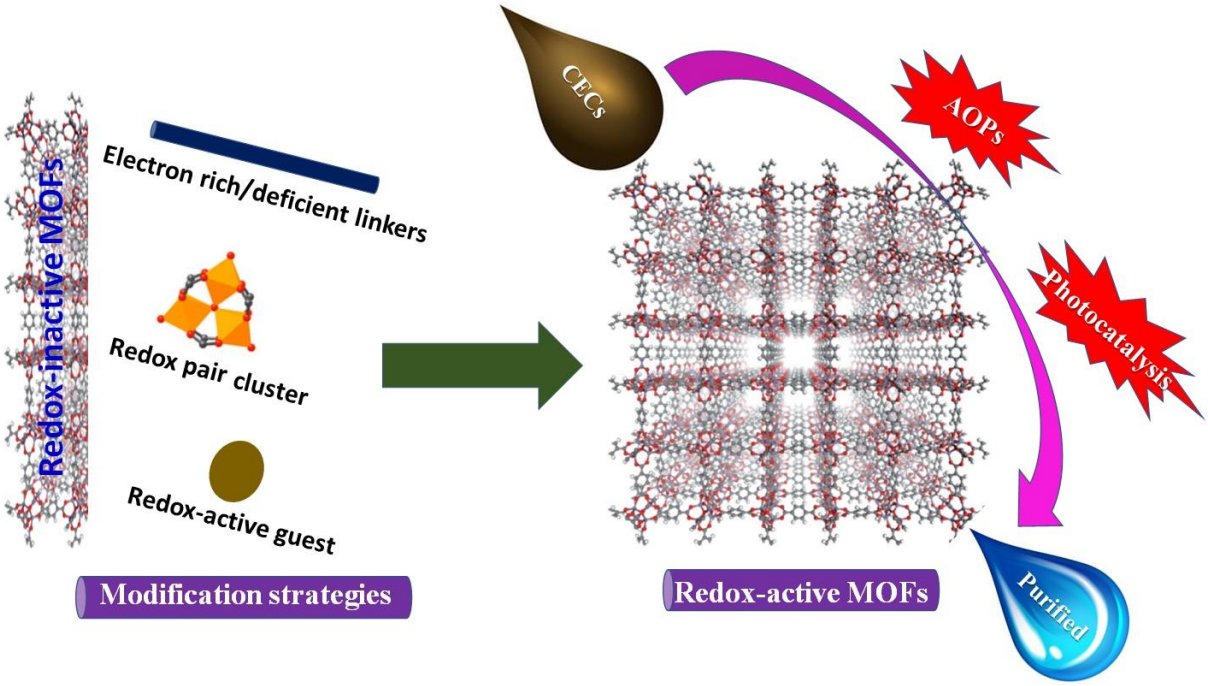

# Redox-active metal-organic frameworks for the removal of contaminants of emerging concern

Chizoba I. Ezugwu*[a], Jayesh M Sonawane[b,c], Roberto Rosal[a]

[a]Department of Analytical Chemistry, Physical Chemistry, and Chemical Engineering, University of Alcala, E-28871 Madrid, Spain.

[b]Department of Chemical Engineering and Applied Chemistry and Centre for Global Engineering, University of Toronto, Toronto, Ontario M5S 3E5, Canada

[c]Department of Chemistry, Laval University, Alexandre-Vachon Pavilion, Quebec (Quebec) G1V 0A6, Canada

*Corresponding author: chizoba.ezugwu@uah.es

## Abstract

The pollution due to the presence of contaminants of emerging concern (CECs) is a major cause for concern because of the serious threat it supposes to human health and ecosystem functions. Many efforts have been geared toward their removal to guarantee safer freshwater. Metal-organic frameworks (MOFs) are crystalline hybrid materials with high surface area and flexible rational design, which allows the incorporation of different active sites into a particular framework, thereby emerging as a potentially excellent candidate for water and wastewater treatment. Benefiting from the unique redox-active properties of MOFs, this review surveys literature update on their application for the removal of CECs. The underlaying electron transfer mechanism and strategies for incorporating redox-active sites into MOFs are comprehensively discussed. Different components of MOFs that are redox-active are further highlighted. This study elaborates the application of MOFs for Fenton-type and other advanced oxidation processes (AOPs) for removing emerging contaminants. AOPs generate highly reactive strong oxidants like hydroxyl and sulfate radicals that are efficient for degrading emerging pollutants with high mineralization rates. MOFs display semiconductor-like properties. Their photocatalytic use for the removal of dissolved emerging pollutants is detailed in the discussion. This review also provides an overview of the most promising directions for future research.

**Keywords:** Metal-organic frameworks, redox activities, emerging contaminants, advanced oxidation processes, photocatalysis, water pollution

## 1. Introduction

Until now, water pollution remains a significant challenge for the environment, and continuous research is in progress on tackling this problem. Environmental pollution is incessantly increasing mainly due to anthropogenic activities, such as waste disposal, consumer activities, and accidental or purposeful releases. The term contaminants of emerging concern (CECs) refer to a wide list of compounds defined as a residual category in the sense that they pose a chemical risk to human or the entire ecological health, but they are not monitored or regulated in the environment [1, 2]. The toxicological effects of traditional pollutants have been well studied over the decades, whereas CECs are recently causing widespread concern due to their effects and persistence in the environment [3]. Furthermore, unlike traditional pollutants, CECs are rarely regulated globally [4]. Evaluating the concentration of CECs in aquatic organism can be used as an indicator to access their transformation in the food chain, which in turns significantly reveals the extent of their risk to human health [5]. They are found as hundreds polluting water resources, in fact, they are among the major water contaminants and are mainly released from agricultural, industrial waste, hospital effluents, septic tanks, and other anthropogenic activities. CEC category is continuously expanding with new chemicals that include (but are not limited to) pharmaceuticals and personal care products (PPCPs), pesticides, flame retardants, trinitrotoluene, polybrominated biphenyls, endocrine-disrupting compounds (EDCs), trichloropropane, dioxane, dinitrotoluene, and many industrial chemicals like surfactants, dyes and solvents [6]. After many years of usage of these substances and the realization that they may be harmful to the ecosystem, some were banned and replaced with environmentally friendly chemicals. Consequently, there is a constant change in the composition of inorganic and organic compounds discharged into the environment. The categorization of a compound as CEC may change quickly; hence, the topic is highly dynamic. They may be pre-existing contaminants or newly emerging chemicals with novel negative environmental effects [7].

The adsorption onto suitable materials is a widely explored technology for the removal of CECs. Some limitations of traditional microporous materials, such as activated carbon and zeolites, that are useful in industrial applications, inspired synthetic chemists to design hybrid microporous materials with improved properties for interacting with organic pollutants [8]. For instance, the purely microporous network of zeolites (pore < 1 nm) frequently makes it difficult for the reactants to transport to the active sites, i.e., intracrystalline diffusion limitations. Moreover, their pore surface cannot be easily tailored. Metal-organic frameworks (MOFs), as an emerging class of distinctive porous crystalline materials synthesized

by assembling metal ions/clusters and organic linkers, have gained great attention for their remarkable properties such as large pore volume, open metal sites or coordinatively unsaturated sites, high surface area, easy functionalization and host-guest interactions [9]. Multi-dentate ligands are important for the formation of MOFs since a continuous chain is crucial to achieve crystalline frameworks [10, 11]. Moreover, the framework can further be functionalized via pre- or post-synthetic approaches [12]. Unlike the traditional adsorbents, MOF materials have unique performance advantages, such as controllable structure and modified pore environment, which make the new porous material popular in various fields. As a result, they have demonstrated their potential wide applications in gas storage/absorption [13, 14], catalysis [15, 16], drug delivery [17], and dye/contaminants adsorption [18]. In addition, MOFs possess some promising properties for the removal of CECs such as high sorption capacities, accessible active sites for the chemisorption or degradation of pollutants and their cavities can easily be functionalized to enhance host-guest interaction [7].

In general, the principle of redox processes has been employed to build different materials for industrial applications. Most traditional MOFs have a wide bandgap, making them redox-inactive, while MOFs that are redox active normally contains high concentration of loosely bound charge carriers with accessible redox couples. The redox chemistry of MOFs is a recent research area that gained attention since the detailed understanding of their properties can be useful for designing improved materials with tailored properties [19]. Unlike molecular transition metal complexes, the charge transfer in MOFs takes place in the three-dimensional coordination space, and the presence of cavities provides more opportunity to exploit their host-guest chemistry. Redox-active MOFs are generated either by using redox-active ligands [20] or metals during their synthesis or post-synthetic incorporation of the redox-active guest into the frameworks. The existence of several oxidation states in transition metals ions gives more opportunities for modulating the redox activities in the metal nodes and linker orientation, like π-π stacking, which can be used to engineer charge transfer within the frameworks. To synthesize redox-active framework in their distinct electronic states, there is a need for appropriate oxidants or reductants that would not affect the overall stability of the MOFs. These oxidants or reductants can react with electron-deficient or electron-rich linker, respectively, thereby initiating the redox process [21].

In recent time, some reviews have been published on applying MOFs and their derivatives for the treatment of wastewater. For example, Yamauchi and co-workers reported the application of MOFs together with their derived materials for particularly, sulfate radicals-based advanced oxidation process in treatment of wastewater [22]. As Huang et al. summarized the use of MOF derivatives in advanced oxidation process [23], Sharma and Feng emphasized on MOFs for the same process [24]. However, a review on

employing MOFs that are redox-active for degrading contaminates of emerging concerns, which poses risk to human, are still missing in literature. Different treatment technologies for the removal of CECs such as membranes filtration, ozonation and activated carbon are associated with some drawbacks. For examples, membranes filtration requires high energy consumption due to the high operational pressures and also cost of always replacing the membranes associated to fouling problems [25]. Furthermore, using ozonation results in the generation of some unintended toxic by-products such as bromate, a genotoxic carcinogen [26]. However, the treatment of CECs by advanced oxidation processes (AOPs) generates highly reactive strong oxidants which deplete the pollutants with high mineralization rate, thus reducing the formation of toxic by-product.

In this review, we compiled detailed literature on the applications of redox-active MOFs to treat contaminants of emerging concern, i.e., by advanced oxidation processes technique. Hopping transport and band transport are clarified as the fundamental mechanism of charge transfer in redox-active MOFs. The strategies of incorporating redox-active sites into MOFs, which consist of using electron rich or deficient linker, accessible redox pairs metal clusters and redox-active guest, are also summarized. The components of MOFs that can participate in the redox process are provided. We discussed the potentials of MOFs in advanced oxidation processes to generate hydroxyl radicals ($HO^{\cdot}$), superoxide sulfate or chlorine radicals for the depletion of phthalates, herbicides, insecticides, phenols, dyes and PPCPs. This work is mainly based on recent advancements in the area; thus, we largely restricted our studies to literature reported in the past 5 years and this vital research area is still in its infancy, as illustrated in Fig. 1. This survey will be useful to environmental and materials scientists together with the design engineers.

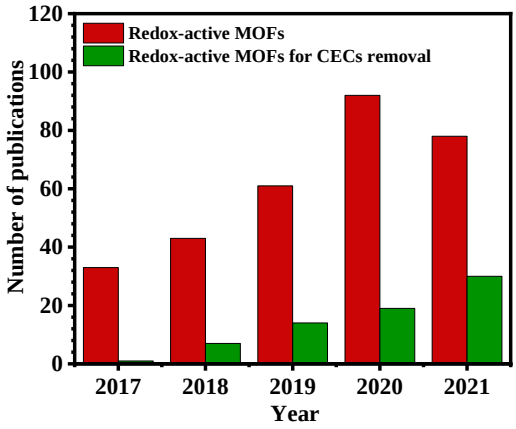


Fig. 1. The current research trends of redox-active MOFs for the treatment of emerging contaminants (the data from Web of Science, Nov. 2021)

## 2. Concepts and redox activities in MOFs

Conductivity in MOFs materials fundamentally depends on the density of charge and electron/charge mobility [27]. In order to achieve high charge density within the framework's structure, a high concentration of loosely bound charge carriers, which emanate from the metal ions and the organic linkers, are required. Traditionally, metal clusters of MOFs are constructed by transition metal ions with vacant or filled d orbital like Zr(IV) or Zn(II), respectively (having inaccessible redox couples), thereby forming

redox-inactive frameworks. In addition, most traditional organic linkers such as carboxylates do not easily transfer electrons between neighboring metal clusters [28]. Therefore, most MOFs reported until relatively recent times have a wide bandgap and, therefore, are redox-inactive. The metal cluster and the organic ligand can be easily engineered to promote redox properties in the MOFs. Electron-deficient and electron-rich ligands can be reduced or oxidized to initiate redox activities in the frameworks. However, the inherent feature of transition metal ions, having several and stable oxidation states, coupled with the possible functionalization of the linker with electron-rich/deficiency entities, offer a plethora of opportunities to construct redox-active MOFs [28]. Redox-active guest species can be incorporated into the pores of the frameworks, and their presence can facilitate charge transfer within the nodes of the frameworks [27]. Charge transfer in redox-active MOFs occurs within three-dimensional coordination space, and these cavities and windows further provide a unique opportunity to exploit host-guest chemistry. The features of MOFs at different redox-state may vary due to their distinct electronic, structural and host-guest properties [19].

### 2.1. Charge transport mechanisms in redox MOFs

Although much work has been carried out on conductive MOFs for different applications, the mechanism of charge transfer within the framework has not been fully elucidated. Owing to MOFs structure's highly ordered crystalline nature, band theory can be employed to investigate their electronic structure [27]. When MOFs gain the required activation energy, electrons and holes (charge carriers) are produced and migrates to the conduction band and the valance band, respectively. The main factors that militate efficient charge transport inside the MOF are the poor conjugation pathway of the organic/inorganic bonding units.

Hopping transport and band transport are the two main charge-transport mechanisms reported in MOFs [28]. As a low-energy charge-transport pathway is required for both mechanisms, a higher orbital overlap improves charge mobility. In hopping transport, localized charge carriers (redox centers) at a specific site with discrete energy level jump between neighboring sites when thermally activated. Charge transport by hopping is often found in disordered materials, such as organic semiconductors and glasses. The propagation of electronic charge is usually accompanied by the movement of charge-compensating ions, i.e., it is a self-exchange process that occurs between electron and their counter-balancing ions. The concentration and identity of ions permeating the frameworks affect the rate of redox hopping. In addition, Marcus's theory of electron transfer can be applied to shed light on redox-hopping [29]. Charge transport in this regime can take place node-to-node, ligand-to-ligand or redox pendant, i.e. attached active redox mediators hopping [30]. The hopping probability between neighboring hopping sites depends on the spatial distance and the energy difference between them [31]. Like Zr-based, redox

inactive metal centers can be rendered active by redox-hopping between periodically arranged equivalent sites [29]. In addition, inactive metal clusters can act as grafting sites for molecular redox couples, and hopping can rely on the linker's features. Redox hopping conductivity can be affected by the topological construction of the MOFs. Maindan et al. investigated the hopping process for four structurally different iron(III) porphyrin containing MOFs, PCN-222(Fe), MOF-525(Fe), NU-902(Fe), and PCN-225(Fe) [32]. These four Zr(IV)-MOFs were designed from iron(III) tetrakis(4-carboxyphenyl)porphyrin, (FeIII)TCPP. The topology and spin-state on the iron-porphyrin center are different, influencing the electron transfer process and the hopping rate. They showed that the hopping rate constant for the $Fe^{III/II}$ reduction depended on the structure in the order of PCN-222(Fe) < MOF-525(Fe) < NU-902(Fe) < PCN-225(Fe).

Unlike the hopping mechanism, electrons in band transport regime are delocalized [33]. Band transport is common in crystalline inorganic materials. In addition, this mechanism occurs in materials having strong covalent bonding, which allows the formation of continuous energy bands [34]. Generally, MOFs materials have low charge mobility, attributed to the small band dispersion and large effective masses. Therefore, in band transport, the charge mobility depends on the frequency of charge scattering events and the effective charge carrier's mass [27]. High charge mobility is achieved with a small effective charge carrier's mass and low density of charge scattering sites. In this mechanism, a rise in temperature results in a conductivity decrease due to increased electron-photon scattering [35]. On the contrary, an increase in temperature promotes conductivity in hopping transport. The temperature-dependent charge transport features of the high charge carrier mobility 2D Cobalt 2,3,6,7,10,11-triphenylenehexathiolate MOFs were investigated [36]. For this MOF, a transition from semiconducting (between 300 and 170 K) to a metallic phase (at temperatures below 130 K) was observed when decreasing temperature, as illustrated in Fig. 2a.

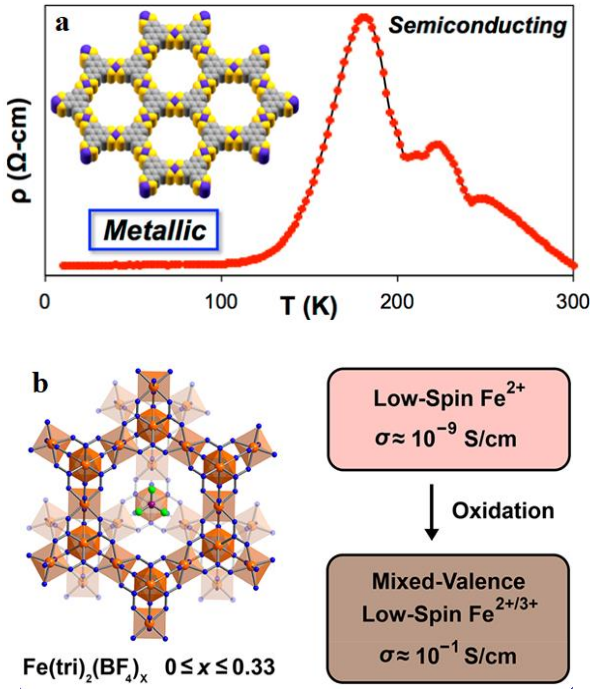


Fig. 2. a) Phase transition with temperature change. Reprinted with permission from [36]. Copyright 2017 American Chemical Society. b) Mixed-valence state in Fe(1,2,3-triazolate)$_2$ framework. Adapted with permission [37]. Copyright 2018 American Chemical Society.

The very high electrical conductivity of this framework was attributed to the efficient overlap between the linker and the metal node frontier orbitals, leading to a better-defined band structure.

An improved charge propagation could be achieved in MOFs by increasing the magnitude of charge delocalization, achievable by π-π stacking and mixed valency. The fundamental feature of mixed valence systems is that either the organic or metal moieties exist in different oxidation states. This property of mixed valency can either be intrinsic or induced by external stimuli, capable of switching the redox states and occurs between close and easily interacting redox-active centers. Murase et al. showed that mixed-valence can improve charge transfer, resulting in higher conductivity and charge delocalization in MOFs and other related systems, such as semiconducting graphene-based materials [38]. It was revealed that Fe(1,2,3-triazolate)$_2$ exhibits very low conductivity in agreement with the insulating character of the low-spin octahedral iron(II) ions bridged by 1,2,3-triazolate units [37]. However, small valence impurities like mixed-valence derivatives showed enhanced charge transport and conductivity, which was eightfold higher than the parent framework, Fig. 2b. The high conductivity was attributed to charge delocalization that occurred between the octahedral low-spin iron(II) and iron(III) centers [37].

Due to the easy tuning of MOF materials, band transport is a more versatile strategy, and more efforts have been made to build highly conductive MOFs by engineering band transport [35]. Fig. 3

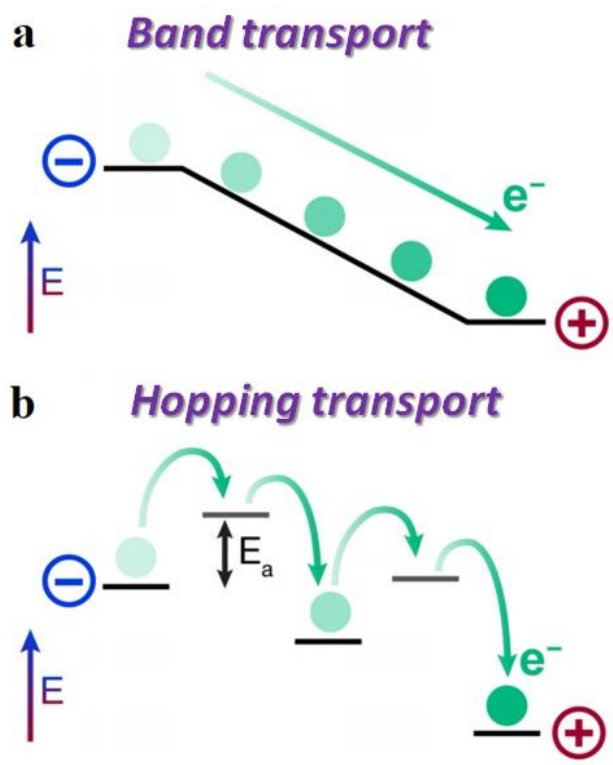


Fig. 3. Charge transport pathways in metal–organic frameworks. Adapted with permission from [34]. Copyright 2020 American Chemical Society.

demonstrates the pathways for two charge transport mechanisms in MOFs.

The two approaches for installing charge-transport pathways in these framework materials are known as “through-bond” and “through-space”. Through-bond always occurs in covalent bonding and facilitates charge transport through the spatial and energetic overlap of the conjugating components. Through-bond charge transport can be instigated in MOFs by incorporating redox-active guests into the framework [39]. These external guest molecules act as bridges between the nearby molecular building blocks [40]. For example, [41] demonstrated that the conductivity in $Cu_3(BTC)_2$

MOF arises from the electron-deficient 7,7,8,8-tetracyanoquinododimethane guest molecule coordinatively interacting with the dimeric Cu subunits via through-bond charge transfer. Large π-conjugated metal–thiolate frameworks synthesized from triphenylene-based ligands can exhibit coplanar through-bond conduction. Combining MOFs with metal nanoclusters and conductive polymers is another way to facilitate electron transfer in the frameworks.

The through-space approach promote charge transport via non-covalent interaction (like π-π stacking) between electroactive components [42]. This type of interaction has been reported in the $(Zn(DMF))_2$(TTFTC)(DPNI) framework between the electron acceptor (DPNI) and electron donor (TTFTC) [43]. As aforementioned, mixed valency is usually reported in MOFs that exhibit through-bond intervalence charge transfer (IVCT) mechanism, such as in the Fe(III) frameworks in which ligand-based IVCT comes from the through-bond interplay between the different redox state of the ligand, 2,5-dihydroxybenzoquinone. Nevertheless, the engineering of 3D MOFs materials that can display a through-space IVCT behavior and utilize the mixed valency to achieve multifunctionality and conductivity has seldom been reported. The IVCT mechanism was recently reported for $[Zn_2(BPPTzTz)_2(tdc)_2]n$, (where BPPTzTz = 2,5-bis(4-(pyridine-4-yl)phenyl)thiazolo[5,4-d]thiazole), in which a mixed-valence state with a new IVCT band in the NIR spectrum appeared [44]. The through-space charge transfer is localized within each cofacial thiazolo[5,4-d]thiazole ligand pair, i.e. localized mixed-valence frameworks. There is intervalence charge transfer due to the mixed-valence state in the framework material.

### 2.2. Strategies for incorporating redox-active sites

Different strategies have been tested for enhancing the redox properties of MOFs, which include pre-, de novo and post-synthetic modification of both the secondary building units (SBUs) and the organic linker. Redox-inactive metal nodes such as Zr-based ones can be activated by substituting the metal ions with electroactive SBUs that contain partially filled d-orbitals, like Cu(I/II) and Fe(II/III) [45-47]. Regarding the organic ligand, carboxylate linkers without other functional units, which are redox-inactive, can be replaced with π-conjugated radicals linkers containing an unpaired electron or redox-active molecules [28, 47]. Redox activation via post-synthetic modification (PSM) [48] strategies has been achieved through ligand exchange and cation exchange. A series of Zr-based-MOFs were synthesized by incorporating the redox-active center in the organic linker using a post-synthetic approach with 2,2′-bipyridine-5,5′-dicarboxylic acid that resulted in Zr-frameworks with N,N′-bis(terphenyl-4,4″-di-carboxylic acid)naphthalenediimide ($H_4$BTD-NDI) linker, which incorporates the NDI redox-active center [49]. Redox activation can also be performed by host-guest PSM using redox-active guests within the framework pores. Furthermore, these guests can

covalently coordinate to the ligand or the metal node.

The redox modulation of frameworks via chemical oxidation with $I_2$ is normally achieved by exposure to iodine which has been reported as a more facile method for the activation of the frameworks [50]. For example, enhanced conductivity of $[Zn_2(TTFTB)(H_2O)_2]$ was realized by chemical oxidation with $I_2$ to give $I_2@[Zn_2(TTFTB)(H_2O)_2]$ [51].

### 2.3. Redox-active sites

#### 2.3.1 Organic linker

The π–π* bands coupled with the extended conjugation system of some organic ligands such as imidazole, pyridine, and thiophene support their electroactivities [52]. Extensive π–n and/or π–π* stacking interactions further stabilize the excited state [53]. Large conjugation or/and delocalization area of ligands facilitates light-induced charge transfer processes, light absorption and luminescent emissions. Notably, in the UV-Vis region, the overlapping bands are due to the highest occupied molecular orbital (HOMO) to the lowest unoccupied molecular orbital (LUMO) transitions, while that for NIR absorption are ascribed to D0→D*n* transition [54]. It has been reported that the redox activity of $Ni_3$(hexaiminotriphenylene)$_2$ framework was due to electron delocalization within the ligand [55].

Among the redox-active linkers, tetrathiafulvalene (TTF, $C_6H_4S_4$) is a promising candidate applied sometimes to prepare conductive multifunctional MOFs materials. TTF has a sulphur-rich conjugated core, which makes it a good electron donor. TTF has two reversible oxidation states, the radical cation ($TTF^+$) and dication ($TTF^{2+}$), which are easily accessible by reactant components [56]. Hence, ligand containing TTF derivatives have been used to prepare not only redox-active frameworks, but redox-switchable MOFs [57, 58]. Notably, the oxidation of TTF to the radical cation or di-cation results in the conversion of the 7π-electron dithiolylidene ring to the 6π-electron conjugated aromatic configuration [57]. Moreover, π...π stacked columns with short S…S interactions exist in TTF core, thereby promoting efficient charge transport. TFT derivatives using carboxylate or nitrogen groups to bridge with the metal via coordination bonds have been used to prepare redox-active MOFs [19].

Leong et al. studied the electronic and optical properties of (TTF)-based MOFs, namely $[M_2(TTFTB)(H_2O)_2]$ (M = Zn, Mn, Co, Cd; TTFTB = tetrathiafulvalene tetrabenzoate), by combined electrochemical and spectroscopic techniques [51]. The arrangement of the linker resulted to both intervalence charge transfer and radical–radical interactions between the mixed pairs of TTFTB linker in the MOFs. Two reversible oxidations potentials due to the $TTF/TTF^+$ and $TTF^+/TTF^{2+}$ were observed. Oxidation of the $[Zn_2(TTFTB)(H_2O)_2]$ (Zn) frameworks resulted in a lower bandgap and increased conductivity from $2.5(2) \times 10^{10}$ S/cm in Zn to $1.6(2) \times 10^9$ S/cm. In another work, four tetrathiafulvalene-tetrabenzoate MOFs with tunable redox-active properties were prepared using Tb, Dy, Ho, and Er [59].

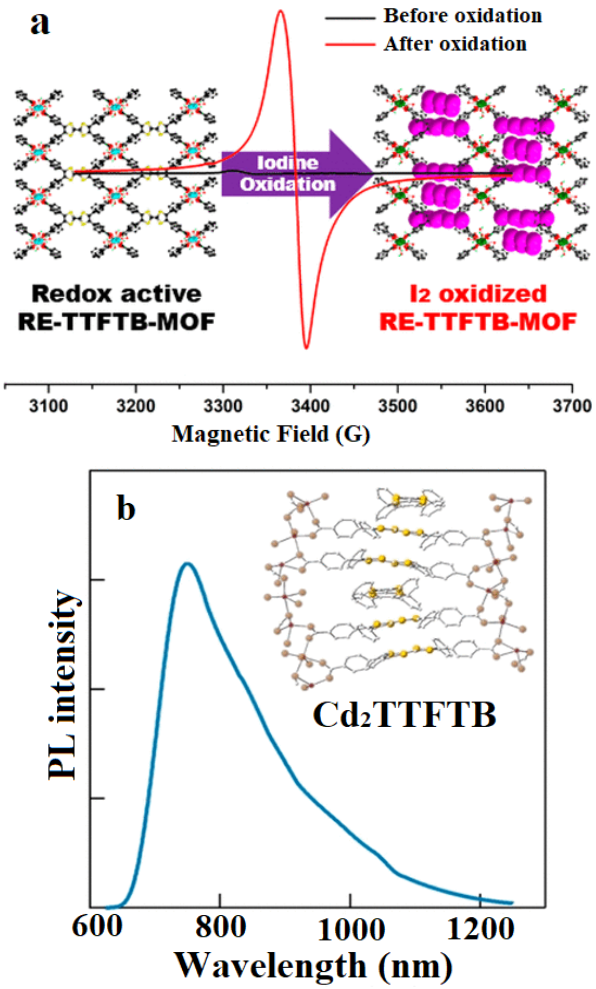


Fig. 4. a) Strong signal ESR spectra in TTF-based MOFs. Reproduced with permission from [59]. Copyright 2019 American Chemical Society. b) Broad-band near-IR spectra in a π-π stacked TTF containing framework. Adapted with permission from [60]. Copyright 2020 American Chemical Society.

As shown by a strong radical signal in the EPR (Fig. 4a), the TTF could be partially oxidized to generated $TTF^{\bullet+}$ using $I_2$. Interestingly, TTF-based MOFs are promising materials for near-IR light emission and can harbor stable radical cation species in the solid state. Wang et al. found a broad-band NIR emission, attributed to $TTF^{\bullet+}$ doublet emission, in the columnar π-π stacked TTF linker (Fig. 4b) [60].

In another work, an extended conjugated analogue of 4,4′-bipyridine with a redox-active TTF moiety, 2,6-bis(4′-pyridyl)-tetrathiafulvalene was selected to assemble 3D$Cu^{I}$-4,4′-bpy-like diamond network [61][. This TTF coordination compound has a high interpenetration (8-fold) with redox-active properties. Dimethylthio-tetrathiafulvalenebicarboxylate and bipyridine ligands (4,4′-bipyridine, 1,2-bis(4-pyridyl)-ethene and 1,2-bis(4-pyridyl)ethane) were used as electron donor and acceptor linkers to prepare 2D manganese coordination MOFs having ligand-to-ligand (TTF-to-bipyridine) charge-transfer [62].

Naphthalenediimides (NDIs) are aromatic n-type organic semiconductors with a robust structure, facile functionalization, and unique redox-activity, thereby endowing them as good candidates for assembling redox-active frameworks. The redox activity of the NDI ligands incorporated into mesoporous Ni-MOFs was used to monitor fluoride in solution via selective and reversible color change upon reduction of the ligand to the radical anions ($NDI^{\bullet-}$) and ($NDI^{2-}$). The production of $NDI^{-}$ and $NDI^{2-}$ depended on fluoride concentration, which resulted in color change of Ni-NDISA MOF [63].

NDI can be substituted with salicylic acid groups to produce N,N′-bis(3-carboxy-4-hydroxyphenyl)-1,4,5,8-naphthalenetetradicarboximide (NDI-bis-salicylate, $H_4$NDISA) that is used to prepare $Mg_2$(NDISA) and $Ni_2$(NDISA) with switchable

color change [64]. Specifically, the quasi-reversible redox events and electrochromic switching of $Mg_2$(NDISA) and $Ni_2$(NDISA) are due to the [NDI]/[NDI]$^{\cdot-}$and [NDI]$^{\cdot-}$/[NDI]$^{2-}$ redox couples.

The topologies of some NDI-based MOFs are prone to interpenetration. Kuang et al. constructed 3D interpenetrated copper-NDI MOFs, $Cu(DPNDI)_2PF_6 \cdot 4DMA \cdot CH_3CN$ (**$Cu^I$-NDI**) (DPNDI = *N*,*N*′-di(4-pyridyl)-1,4,5,8-naphthalenetetra-carboxydiimide), consisting of a linear NDI motif coordinated to Cu(I) center on a diamond topology [65]. The crystal structure analysis revealed that the continuous π-conjugated MOFs assemblies featured J-aggregation, which enhanced electron transport. The π-conjugated aromatic plane provided an electron-hopping pathway along the orientation of the J-aggregation. Combined experimental and DFT calculations indicated that the high electron conduction emerged from π–d coupling and J-aggregation.

Viologen/bipyridinium derivatives are good electron acceptors. Tan et al. used bipyridinium ligand, 1,1′-[1,4-phenylene-bis(methylene)]bis(4,4′-bipyridinium) dichloride, to introduce not only redox-active sites but also Lewis acidic sites into Zn-based MOF, which was applied for ammonia capture over water [66]. In another study, viologen-containing ligand $[H_2L]Cl_2$ ([1,10-bis(4-carboxylatobenzyl)-4,40-bipyridinium] dichloride), was assembled with Co(II) to generate a redox-active reversible redox and photochromic MOFs, Co-MOF-1, for the discriminative detection of alkylamines [67]. The reversible redox coupled with the photochromatic characteristics resulted from photoinduced electron transfer from the oxygen atoms to the viologen moieties. Due to the electron transfer from the electron-rich amine molecules to electron-deficiency viologen linker, these MOFs showed different color changes to different types and molecular sizes of volatile amine vapors [67]. Besides, the color depended on the number of N–H bonds and the size of the substituent of the amine molecules. The incorporation of viologen moieties into a europium-based MOF (Eu-MOF), endowed the framework with both photochromism and photo-modulated fluorescence features [68].

Other organic linkers that impact redox MOF activities include triphenylamine and metalloporphyrins. A triphenylamine (TPA) derivative, 4,4′,4″-Tricarboxytriphenylamine ($H_3TCA$) ligand, was employed for the preparation of an electroactive Ni-MOF [69]. The redox-active ligand acts as the electroactive source, and paramagnetic ordered $Ni_4O_4$ nodes as electronic transport clusters. The redox-active TPA can be used to prepare electroactive frameworks because the combination of paramagnetic metal clusters and electroactive linkers promoted electron transport [69]. With this rationale, large-area electrochromic thin films MOF composites were prepared by electrodeposition, which rapidly changed under electric bias [70].

Incorporating redox-active metal complexes have advantages for fabricating conductive MOFs because of their stable coordination sites and the possibility of establishing a direct connection between the redox sites. Porphyrin moieties in the

ligand provide suitable sites for the coordination of the desired redox-active metal species [71, 72]. A series of metalloporphyrinic MOFs, PCN-222(M) or ($Zr_6(\mu_3\text{-}OH)_8(OH)_8(M\text{-}TCPP)_2$, (M= Mn, Fe, Ni, or H (no metal) and TCPP = tetrakis(4-carboxyphenyl)porphyrin), were prepared and deposited as thin films on carbon fiber paper (CFP) substrates [73]. The electron transport between the porphyrin moieties occurred by a charge hopping mechanism [74]. The electron transport through the film surface depended on the active metal center in the MOFs [73]. Ni thin films had the highest ratio of $M^{2+}$ and the highest electrochemical performance in terms of current density. XPS and XANES proved that $Ni^{2+}$ was oxidized to $Ni^{3+}$, which in turn oxidized $NO^{2-}$ to $NO^{3-}$. In addition, bipyridine [75, 76] and catechol metalloligands [77, 78] have been successfully incorporated as redox-active species into MOFs.

Xu et al. used $(Ru[4,4'\text{-}(HO_2C)_2\text{-}bpy]_2bpy)^{2+}$ and $Zn^{2+}$ to prepare electrochemically stable redox-active MOFs with high electrochemiluminescence due to the electron transfer from the framework to a co-reactant [79]. Based on electrochemical and electrochemiluminescence studies, the addition of tripropylamine (TPrA) to Ru-MOFs enhanced the current from 24 to 72 μA, and there was catalytic oxidation of TPrA by $Ru(bpy)3^{3+}$ to $Ru(bpy)3^{2+}$. The [Ru3þ-MOF] oxidizes tripropylamine to form the $TPrA^{+\cdot}$ active radicals.

### 2.3.2 Inorganic clusters

Redox-active transition metal clusters could be used for the fabrication of functional MOFs provided they are sufficiently stable. Iron-based redox-active centers have been extensively used to generate multifunctional MOFs, with Fe having stable oxidation states of +2 and +3 [80]. Owing to the redox couple that involves the coordinatively unsaturated Fe(II) sites in MIL-100(Fe), the loading of $CuCl_2$ resulted in its reduction to CuCl within the pore of the frameworks, without the assistance of any external reducing agent, as shown in Fig. 5a [81]. Cu(I)-loaded MIL-100(Fe) showed superior $C_3H_6/C_3H_8$ selectivity when compared to Cu loaded into MIL-100(Al), which does not contain redox-active sites indicating that the adsorption selectivity of redox-active MOFs can be enhanced by loading metal ions into the framework. The Fe(II) sites act as a reducing agent for Cu(II) as well as an antioxidant to protect and stabilize the reduced Cu(I) species.

XPS measurements together with DFT calculations, established that the reduction of Cu(II) to Cu(I), created a mixed valency state that influenced the selective adsorption of gas molecules [82]. Invariably, the binding of the adsorbate is a function of the unsaturated metal sites in copper-based MOFs. In another work, the redox reaction of $Cu^{2+}/Cu^{+}$ within Cu-MOF-74 assisted in the reversible adsorption and release of cadmium ions in aqueous solutions [83]. Litvinova et al. employed redox-active rhenium octahedral $[Re_6Se_8(CN)_6]^{4-/3-}$ cluster anions with $Gd^{3+}$ ions and dicarboxylate linkers (furan-2,5-dicarboxylate (fdc) or thiophene-2,5-dicarboxylate (tdc)) to construct multi-component MOFs, $[(Gd(H_2O)_3)_2(fdc)Re_6Se_8(CN)_6]\cdot nH_2O$ and [(Gd-

$(H_2O)_3)_2(tdc)Re_6Se_8(CN)_6]\cdot nH_2O$ that demonstrated excellent $CO_2/N_2$ and $CO_2/CH_4$ selectivity, paramagnetic behavior (typical for $Gd^{3+}$), and red photoluminescence [84]. The treatment of both frameworks with a bromine solution resulted in one-electron oxidation of the cluster unit and the formation of green frameworks, which can be further reduced with a hydrazine solution, thereby restoring the initial MOFs**.**

The interfacial electron transfer from $Cu^+$ to $Fe^{3+}$ was used to fabricate MOFs-derived iron-copper bimetallic composites, FeCu@C [85]. The iron and copper species in the inner bimetallic nanoparticles facilitated the generation of hydroxyl radicals in Fenton reaction for sulfamethazine degradation. [86] employed a redox-active $Ni_2$(dihydroxyterephthalic acid) MOF, also known as CPO-27-$Ni^{II}$, as a sensor for the non-enzymatic detection of glucose. The water-stable CPO-27-$Ni^{II}$ frameworks have a wide pore diameter of ca. 1.1 nm, allowing the glucose molecule (ca. 1 nm) to be adsorbed into its pores [87]. In an alkaline solution, the $Ni^{II}$ in CPO-27-$Ni^{II}$ -modified glassy carbon electrode can easily be oxidized to $Ni^{III}$, forming $Ni^{II}/Ni^{III}$ redox pair, thereby mediating the oxidation of glucose to gluconolactone. The as-prepared sensor shows a wide linear range and a low detection limit [86].

By using MOF-5 as a precursor, a redox-active framework was prepared by partial substitution of Zn(II) by Mn(II) in the $Zn_4O$ metal cluster, as shown in Fig. 5b [88]. The Mn(II) ion was redox-active with a variety of oxidants. For example, reacting the framework with tert-butylsulfonyl-2-iodosylbenzene ($^tBuSO_2PhIO$) produced MnIV-oxo intermediate that can be reduced to MnIII-OH species in contact with adventitious hydrogen. Thus, the SBU of MOFs can constitute high-valent metal-oxo species that are potential catalysts for oxygen atom transfer, acting for example, as a selective catalyst for the epoxidation of cyclopentene [88]. Also, redox transformations can occur in the metal nodes of iron substituted $Zn_4O$(terephthalate)$_3$ that catalyzes the disproportionation of nitric oxide, Fig. 5c [89]. The high spin configuration of the iron sites in the $Fe^{2+}$-MOF-5 activated NO, and the disproportionation mechanism was based on a single iron atom.

Redox activity and electrical conductivity are present in the ferrocenyl phosphonate structural unit. Consequently, bimetallic MOFs containing the stable ferrocene moiety and another metal like Ni or Co generate redox frameworks with redox activities. Two 3D Ni and Co redox-active MOFs based on ligands, ferrocenyl diphosphinate and 4,4'-bipyridine, were prepared and explored as stable electrocatalysts in hydrogen evolution reactions (HER) [90]. From the electrochemical studies, Ni-MOF exhibited more favorable reaction kinetics than Co-MOF; thus Ni-MOF has better HER performance.

Chromium(II) sulfate, potassium 1,3,5-benzenetricarboxylate or potassium 4,4′-(hexafluoroisopropylidene)bisbenzoate were utilized to prepare single-crystalline chromium(II)

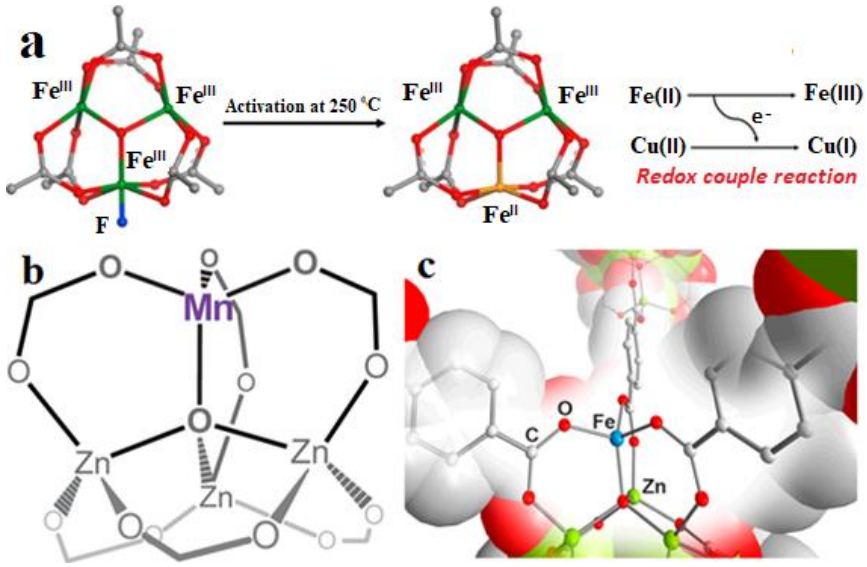


Fig. 5 a) Reduction of one of the three coordinatively unsaturated Fe(III) sites at 250 °C and formation of redox couple by incorporation of $CuCl_2$. Reprinted with permission from [81]. Copyright 2018 Elsevier. b) $Zn^{2+}$ ions substituted $Mn^{2+}$ in MOF-5 cluster. Reproduced with permission from [88]. Copyright 2018 American Chemical Society. c) SBUs of MOF-5 with one $Fe^{2+}$ substituting one $Zn^{2+}$ ion. Reproduced with permission from [89]. Copyright 2015 American Chemical Society.

carboxylate MOFs in water under room temperature [91]. The redox properties of these MOFs, $Cr_3(BTC)_2{\cdot}3H_2O$ (BTC = 1,3,5-benzene-tricarboxylate), Cr(hfipbb)·$H_2O$ (hfipbb = 4,4′-(hexafluoroisopropylidene)bisbenzoate) and their dehydrated counterparts, $Cr_3(BTC)_2$ and Cr(hfipbb) were studied by cyclic voltammetry, showing oxidation/reduction pathways assigned to $Cr^{II}/Cr^{III}$, $Cr^{III}/Cr^{IV}$ and $Cr^{III}/Cr^{V}$. Therefore, Cr centers in the Cr(II)-carboxylate MOFs can reversibly adopt multiple oxidation states.

### 2.3.3 Inorganic cluster and ligands

The coexistence of redox-active sites both in the metal clusters and the organic ligand is another strategy to improve charge transport within the framework structure. A triphenylamine-based MOFs, Cu-TCA ($H_3TCA$ = tricarboxytriphenyl amine), exhibited redox activities both in the organic ligand radicals ($N/N^+$) and the metal clusters ($Cu^+/Cu^{2+}$), which were confirmed by both electrochemical results [92]. A challenge for the practical application of this kind of MOFs is that they have short cycling life, and sometimes their working voltage is not high enough. In another work, Zhang et al. used *In situ* XANES analysis and cyclic voltammetry to reveal that both the anthraquinone groups and the Cu ions in Cu(2,7-AQDC) MOFs, where $H_2AQDC$=2,7-anthraquinonedicarboxylic acid, displayed reversible redox activities [93].

### 2.3.4 Redox-active guests

Small metal nanoparticles can be confined into the pores of the framework. Post-synthetic functionalization approach was used to incorporate bistable mechanically interlocked molecules into NU-1000 [94]. Cyclic voltammetry and solid-state UV-vis-NIR reflectance spectroscopy revealed that these bistable [2]catenanes, $FC^{4+}$, retained their reversible redox-switching properties inside the nanopores of the Zr-based MOF. Liu et al. encapsulated ferrocene molecules into the cavities of UiO-67 using a solvent-free evaporation method to prepare a ferrocene@UiO-67 composite with ferromagnetic behavior at room temperature [95]. The CV curves for the ferrocene@UiO-67 composite showed a pair of symmetric redox peaks assigned to the reversible conversion between $Fe^{2+}$ and $Fe^{3+}$ of ferrocene in the UiO-67 framework but no peak was observed in blank glassy carbon electrode and the pristine UiO-67.

Furthermore, redox-active dyes can be absorbed by MOFs to activate the frameworks. Halls et al. loaded methylene blue (MB) in the pores of [Zn4O(bdc)$(btb)_{4/3}$], also known as UMCM-1, (bdc = 1,4-benzenedicarboxylate, btb = 1,3,5-benzenetribenzoate) [96]. The adsorbed dye retained its redox-active when bounded inside of the UMCM-1 host structure. Electron hopping conduction are influenced by the pH and improved internal charge transport are observed in alkaline environments. This was explained based on faster single electron hopping transport in pores.

## 3. Strategies for using redox-active MOFs for the treatment of emerging pollutants

Redox properties are normally correlated with the catalytic ability of the MOFs. The nature and strength of the redox pair of MOFs situated in the metal cluster, functionalized linker or the interacting guest influences the overall performance of the frameworks for the removal of CECs. The synergy between the redox pair and the high surface area/porosity of MOF materials are appealing for their catalytic efficiency. Like iron-containing MOFs are getting more interest as a heterogenous Fenton catalyst because of the synergy between the Fe(II)/Fe(III) redox pair and the high porosity for the adsorption/oxidation of the organic pollutants. Regarding the structure-performance relationship; the content of the exposed and accessible redox-active metal sites influences their removal efficiency. Liao et al. revealed that three different structural kinds of MIL-88A-Fe (rod-like, spindle-like and diamond-like structures) with varied Fe contents exhibited different phenol degradation efficiencies [97]. Compared to the other two, rod-like MIL-88A-Fe showed the highest turn-over frequency value (5.0 $h^{-1}$), i.e., favored Fenton-like activity, attributed to its highest content of accessible exposed Fe surface species.

Advanced oxidation processes have been adopted to remove emerging pollutants because of their high efficiency, low cost, and environmentally benign [98]. Nevertheless, the efficiency of existing catalysts remains unsatisfactory, for example, fast charge recombination in photocatalytic materials.

Therefore, recent interest focuses on using advanced hybrid materials to achieve improved degradation efficiency. MOFs-based AOPs such as Fanton-like processes, sulfate radical mediated oxidations and photocatalysis are recently gaining high attention for the treatment of emerging pollutants due to their reproducibility, simplicity and high catalytic efficiency [7, 24].

### 3.1. Advanced oxidation processes for the removal of aqueous pollutants

Organic anthropogenic pollutants are widely distributed in all environments. A huge variety of organic pollutants are constantly emitted to the atmosphere, inland waters, and oceans, where they partition among vapor, liquid and solid phases according to their volatility, solubility and affinity with different substrates. Adsorption is generally considered a suitable technology for removing gas and aqueous streams because of its simple design, low energy consumption and high removal capacity with no by-product formation [99, 100]. A plethora of materials can be used as adsorbents, from the well-known activated carbons, zeolites or clay minerals to industrial by-products or biosorbents. The high porosity and surface area of MOFs combined with their tunable chemical specificity make them excellent candidates for many adsorption applications [101]. It has been well described that MOFs showed outstanding properties for gas storage, heterogeneous catalysis, and biomedical applications [102]. Their flexibility in terms of chemical functionalization and pore size make them excellent adsorbents favorably competing in capacity and kinetics with conventional materials [103]. Adsorption mechanisms include electrostatic, acid-base, hydrophobic interactions, π-π interactions and H-bonding [104, 105]. Besides, their flexible structure may enhance intraparticle diffusion by the so-called breathing effect [106].

MOFs have great potential as effective adsorbents for emerging aqueous pollutants [105]. The adsorption of several nonsteroidal anti-inflammatory drugs on Zr(IV)-based MOFs (UiO-66 and MOF-808) showed good capacity due to the chemical interaction of anionic drugs with the incompletely coordinated cationic Zr and to the π–π interaction between benzene rings in drugs and ligand [107]. The selective removal of PPCPs is favored by implementing functional groups that promote adsorption [108]. Accordingly, the functionalization of MIL-101 by –OH, $–NO_2$, and $–NH_2$ groups to enhance specific interactions like H-bonding was found to improve sorption capacity and kinetics [109, 110]. Surface grafting of MIL-101(Cr) with urea or melamine was explored to enhance the adsorption of nitroimidazole antibiotics by favoring H-bonding between the nitro groups of antibiotics and the amines introduced via grafting [111]. In other cases, MOFs have been pyrolyzed to obtain highly porous carbons tested as adsorbents for different compounds, including PPCPs [112, 113]. The separation of MOFs after use has been addressed using different strategies. Zhuo et al. prepared MIL-101(Cr)/sodium alginate and MIL-101(Cr)/chitosan composite beads for the

adsorptive removal of benzoic acid, ibuprofen and ketoprofen, which proceeded by electrostatic and π-πinteractions. After use, composite beads, with 2-3 mm diameter, could be easy separated by filtration, overcoming one of the main difficulties for MOF recycling [114]. Also, photocatalytic MOFs based heterojunctions were used for the degradation of ibuprofen [115]. Another usual strategy is creating magnetic materials, which allows easy separation by external magnetic fields [116-118].

Advanced oxidation processes are characterized by the in-situ generation of highly reactive strong oxidants, especially hydroxyl radicals ($HO^{\cdot}$), but also other oxidizing species such as superoxide sulfate or chlorine radicals [119]. AOP constitutes a wide family comprising various technologies that include well-established methods such as those based on ozone and ultraviolet irradiation, the family of Fenton processes, and many other catalytic, electrochemical and ultrasound-based methods under different stages of development [120]. The high reactivity provided by AOP allows depletion of organic pollutants with high mineralization rates and, therefore, reducing the formation of toxic reaction by-products [121]. Some AOPs have been tested in catalytic processes involving MOFs, generally exploiting in parallel their redox capacity and their physicochemical with organic substrates. Most reported MOF-based AOP produce hydroxyl radicals from the decomposition of $H_2O_2$, including heterogeneous Fenton and photo-Fenton, or sulfate radicals from persulfate (also named peroxydisulfate, PS, $S_2O_8^{2-}$) or peroxymonosulfate (PMS, $HSO_5^-$). MOFs have been tested for the oxidation of several emerging pollutants in water solutions. The list includes plasticizers (phthalates), pesticides (herbicides, insecticides), industrial chemicals (phenols, industrial dyes) and PPCPs (antibiotics, lipid regulators, anti-inflammatories).

### 3.1.1. MOFs-based heterogeneous Fenton-like processes

Fenton systems involve the decomposition of $H_2O_2$ catalyzed by Fe(II) to yield hydroxyl radicals. Under acidic conditions, pH ~ 3, in homogeneous systems, the reaction becomes catalytic because the Fe(III) produced is converted back to Fe(II) by more $H_2O_2$ with the production of hydroperoxide radicals ($HOO^{\cdot}$). Heterogeneous Fenton systems decompose $H_2O_2$ using and surface redox pair Fe(II)-Fe(III), which produce hydroxyl and hydroperoxide radicals in the same way as homogeneous Fenton with the advantage of the easy separation of heterogenous catalysts. Generally, heterogeneous Fenton catalysts are porous materials that adsorb pollutants, thereby enhancing the degradation rate. Another advantage of heterogeneous systems is that they are efficient over a wider range of pH values [122-124]. Iron-based MOFs are appealing for heterogeneous Fenton because they favorably combine the presence of active iron sites with the adsorption mechanisms that favor interaction with organic compounds. Accordingly, most MOFs used for heterogeneous Fenton are Fe-based or Fe-containing hybrid composites [125]. Some of them showed excellent catalytic activity for the oxidation

of aqueous pollutants [126], but their application is still scarce and mainly focused on model pollutants like phenol or industrial dyes [24].

In many cases, MOF for Fenton-like processes enhanced their activity by incorporating additional active sites [127]. Accordingly, multi-metallic MOF are becoming a hot topic for oxidation catalysts. The isomorphic substitution of iron in Fe(BDC)(DMF,F) (BDC = terephthalic acid), a MIL-53 type material, by manganese, cobalt, and nickel was explored for the degradation of phenol. It was showed that the incorporation of Mn increased the degradation efficiency under Fenton-like conditions, the activity being essentially determined by Fe/Mn ratio [128]. Similarly, BiOCl/MIL-100(Fe) hybrid composites exhibited better RhB degradation efficiency than BiOCl and MIL-100(Fe) [125]. The enhanced activity was mainly ascribed to the presence of coordinatively unsaturated iron centers $Fe^{2+}/Fe^{3+}$ and efficient charge carrier separation. Moreover, the underlaying reaction mechanisms showed that $^{\cdot}OH$ and $h^{+}$ were the main active species. Wang et al. were able to use mcro-sized Fe-MOF sheet to remove chloroquine phosphate from water with $^{\cdot}OH$ as the primary reactive specie [129]. One drawback of Fe-MOF catalysts is that they possess Fe(III) instead of Fe(II) sites, limiting their Fenton catalytic activity. Lv et al. introduced Fe(II) onto MIL-100(Fe) to created Fe(II)@MIL-100(Fe) material with high capacity (~70 % in 3 h) for the decomposition of the dye methylene blue over a wide pH range of 3–8 [130]. It has been suggested that the combined presence of Fe(II) and Fe(III) may enhance the production of ·OH radicals. However, the leaching of ferrous ions during Fenton reaction results in a loss of active phase from Fe(II)@MIL-100(Fe) catalyst; another disadvantage common to many heterogeneous Fenton catalysts was the limited mineralization extent [130]. Other authors studied Fe-based MOFs for heterogeneous Fenton reactions. PMS activation was achieved using CuS@MIL-101(Fe), which was applied to degrade up to 100.0% of coumarin (30 μM) in 10 min. The high catalytic activity was attributed to the synergistic effect of redox pairs of $Fe^{3+}/Fe^{2+}$, $Cu^{+}/Cu^{2+}$, $S^{2-}/S_2^{2-}/S^0$ sulfate species and the presence of the sulfur vacancies [131].

The catalytic performance of MIL-53(Fe) and Fe(BDC)(DMF,F) was studied using phenol degradation at neutral pH. The better activity of Fe(BDC)(DMF,F) was attributed Fe(II) in its framework. Phenol was almost completely decomposed in 3 hours with high (79 %) mineralization rate [132]. Nanoscale Fe(II)-bpydc was also shown to activate $H_2O_2$ to degrade phenol with good activity at pH in the 3-5 range but poor stability because yield substantially decreased during the first three reaction cycles [133].

Attempting to overcome these drawbacks, bimetallic catalysts have also been proposed by some groups. Iron-copper bimetallic MOF, $Fe_xCu_{1-x}$(BDC), prepared by a solvothermal method, was used to degrade sulfamethoxazole with hydrogen peroxide. The catalyst worked over a wide pH range with high activity attributed to the synergistic effect between Fe and Cu [134]. It was shown that

the catalytic reaction occurred on the surface of $Fe_xCu_{1-x}$(BDC), the Fe(II) sites providing the electrons to produce $HO^{\cdot}$ from $H_2O_2$ decomposition; Fe(III) sites would capture one electron from $H_2O_2$ to $HOO^{\cdot}$ yielding back Fe(II). The possible mechanism is shown in Fig. 6. According to it, Cu(II) sites also catalyze $H_2O_2$ decomposition to $HOO^{\cdot}$ and Cu(I). According to thermodynamics, Cu(I) could regenerate Fe(II) through electron transfer. Sulfamethoxazole are oxidized by surface-bound $HO^{\cdot}$ [134].

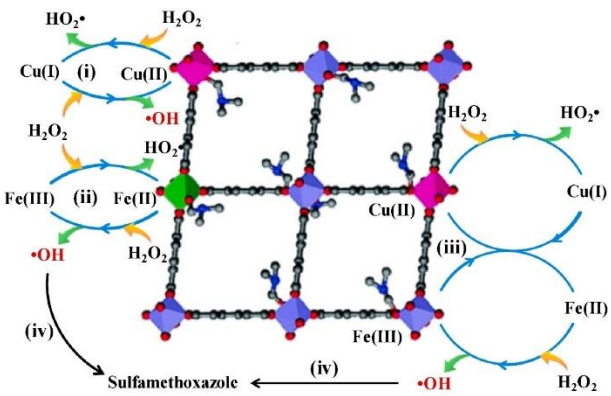


Fig. 6. Proposed reaction mechanism for the degradation of sulfamethoxazole by $Fe_{0.75}Cu_{0.25}$(BDC)/$H_2O_2$ system. Reproduced with permission from [134]. Copyright 2020 Elsevier.

Photo-Fenton benefits from UV or visible light irradiation to generate additional oxidant radicals from $H_2O_2$ or the decomposition of Fe-(OH) species [135]. MIL-53(Fe) exhibited high photocatalytic activity under visible light irradiation for the degradation of clofibric acid and carbamazepine [136]. Liang et al. showed that Pd@MIL-100(Fe) can be used as efficient photo-Fenton catalyst for removing PPCPs, namely ibuprofen, bisphenol A and theophylline using visible light produced by a Xe-Arc lamp [137]. The photoactivity of Pd@MIL-100(Fe) was attributed to charge-carrier separation in Pd@MIL-100(Fe) with respect to MIL-100(Fe). In a more recent work, the same group prepared Pd-nanoparticle-decorated phosphotungstic acid (PTA)-MIL-100(Fe) nanocomposites, Pd-$H_3PW_{12}O_{40}$-MIL-100(Fe). It is a ternary hybrid in which PTA encapsulated during MOF synthesis serves as a reducing agent and stabilizer for Pd nanoparticles. The material was used for the photo-Fenton degradation of theophylline and ibuprofen under visible light irradiation. The enhanced photocatalytic performance was attributed to the capacity of Pd nanoparticles to accept electrons from MIL-100(Fe). Besides, the presence of Pd nanoparticles combined with PTA promotes electron transfer by accepting photogenerated electrons in the conduction band of PTA and from it to Pd nanoparticles [138]. In another work, redox-active linker, tetrathiafulvalene, was used to prepare a silver nanoparticles-doped Zr-MOF, which was efficiently for photocatalytic degradation of sulfamethoxazole [139]. Vu et al. incorporated iron atoms into Cr-MIL-101 MOF using a hydrothermal method [140]. The material, in which Fe substituted about 25% of Cr, showed good stability (iron leaching 1.5 mg/L after 90 min) and activity for the photo-Fenton degradation of reactive dye RR195.

The incorporation of carbon-based nanomaterials was explored to provide a higher efficiency by exploiting heterojunctions for improving charge carrier mobility and to get more

environment-stable catalysts. Qin et al. assembled iron-carbon nanoparticles to the coordinatively unsaturated Cr sites of MIL-101(Cr) using citric acid as a chelating agent [141]. They could prepare MOFs (iron percent < 3.86 %) without agglomeration on their external surface to be used as catalysis for photo-Fenton reaction at neutral pH displaying high activity for $H_2O_2$ activation, which was attributed to [Fe–O–C] sites inside MIL-101 [141]. $Cu_2O$/MIL(Fe/Cu) composite prepared via in situ Cu-bridging was used for the photo-Fenton degradation of thiacloprid. $Cu_2O$ grew on the surface of MOF, and Cu-bridge promoted an intimate interface with the MOF, which accelerated charge transfer to Fenton-generated radicals [142]. The incorporation of graphene oxide (9.0 wt%) to the surface of MIL-88A(Fe) enhanced the degradation of rhodamine B (RhB) to reach complete conversion even after five reaction cycles. The reason may be that the surface heterojunction Fe-MOF-GO enhances photon-induced charge separation due to the role of GO as an electron acceptor. Photogenerated electrons on GO produce $HO^{\cdot}$ from $H_2O_2$; holes can directly oxidize RhB and Fe(III)-O clusters on the surface would also decompose $H_2O_2$ to produce more $HO^{\cdot}$ by Fenton-like mechanism [143]. MOF heterojunction was also explored for photo-Fenton degradation of MB using g-$C_3N_4$/$NH_2$-MIL-88B(Fe) composites [144]. Their higher efficiency was attributed to $H_2O_2$ decomposition by photo-induced electrons facilitated by the g-$C_3N_4$-MOF heterojunction. Additionally, the so-prepared composites displayed good reusability and stability. Photo-electro-Fenton was explored by means of MOF(Fe-Co)/Carbon aerogel cathodes. With an optimal Fe:Co ratio 2:1, in situ generation and decomposition of $H_2O_2$ allowed producing $HO^{\cdot}$ from photoinduced electrons. The efficiency was pH-independent and was sufficient to degrade RhB (100 %) and dimethyl phthalate (85 %) in < 120 min with very low metal leaching [145]. A summary of MOFs, substrates and reaction conditions for articles recently published on the use of heterogeneous Fenton-like processes is shown in Table 1.

**Table 1.** Fenton-like processes for the removal of emerging aqueous pollutants

| MOFs | Characterization properties | Reaction | Reaction conditions | Redox properties/ potentials | Ref. |
|---|---|---|---|---|---|
| Fe(II)@MIL-100(Fe) | 1228 $m^2$/g; pore volume 0.61 $cm^3$/g; pore diameter < 20 nm | Heterogeneous Fenton | Catalyst 1 g/L; methylene blue, 500 mg/L; TOC removal < 30 % in 8 h; 40 mM $H_2O_2$; pH 3-8 | $H_2$-TPR profile with peaks shifted to lower temp. after Fe(II) loading | [130] |
| MIL-53(Fe) and Fe(BDC)(DMF,F) | Particles of irregular shape, ~ 5 μm; | Heterogeneous Fenton | Catalyst 160 mg/L; phenol 1000 mg/L; phenol conversion > 99 | Fe Mössbauer spectrometry | [132] |

| | | | | | |
|---|---|---|---|---|---|
| | textural details not given | | % in 3 h; $H_2O_2$: phenol mol ratio 14:1; initial pH 6.2 | detecting % spin state of Fe(II)/Fe(III) | |
| Fe(BDC)(DMF,F) (Mn, Co, Ni) | Triangular prims morphology about 10 µm width; no textural parameters given | Heterogeneous Fenton | Catalyst 320 mg/L; phenol 1000 mg/L; conversion 65.3-75.9 % in 180 min; $H_2O_2$:phenol mol ratio 14:1; pH 6.2 | Standard reduction potential; Fe(II)/ Fe(II) = 0.77 V, Mn(III)/Mn(II) = 1.51 V, Fe(II) + Mn(III)/ Fe(III) + Mn(II) = 0.73 V | [128] |
| $Fe_xCu_{1-x}$(BDC) | $Fe_{0.80}Cu_{0.20}$(BDC) 265 $m^2$/g; average pore diameter 7 nm | Heterogeneous Fenton | Catalyst 500 mg/L; sulfamethoxazole, 20 mg/L;100 % removal in 120 min; $H_2O_2$ 6 mM; pH 3-11 | Standard reduction potential; ($Cu^{2+}/Cu^{+}$) = 0.17 V); ($Fe^{3+}/Fe^{2+}$) = 0.77 V; $Cu^{+}$ + $Fe^{3+}$/ $Cu^{2+}$ + $Fe^{2+}$ = 0.6 V | [134] |
| MIL-53(Fe) | 184 $m^2$/g; Band-gap energy 2.88 V vs. NHE | Photo-Fenton; Xe-lamp λ > 420 nm | Catalyst 100 mg/L; clofibric acid, carbamazepine, 40 mg/L; 80-90 % removal after 4.5 h; 1 ml 30%$H_2O_2$/L | Flatband potential of MIL-53(Fe) = -0.6 V | [136] |
| Fe-Cr-MIL 101 | 2297 $m^2$/g; av. pore diameter 2 nm | Photo-Fenton; UV-A lamps 400-800 nm | Catalyst 300 mg/L; RR195, 100 mg/L; 100 % conversion for 100 min; 136 mg $H_2O_2$/L; pH 5.5 | XPS spectra for the oxidation states of Fe | [140] |
| Pd@MIL-100(Fe) | 2102 $m^2$/g; pore diameter 4-12 nm | Photo-Fenton; Xe lamp λ ≥ 420 nm) | Catalyst 125 mg/L; theophylline, ibuprofen and bisphenol A, 20 mg/L; TOC removal 20.5-69.2 %; 1 mL $H_2O_2$/L; pH 4 | Band gap energy 2.41 V vs. NHE | [137] |
| Pd-$H_3PW_{12}O_{40}$-MIL-100(Fe) | 825 $m^2$/g; pore volume 0.41 cm3/g | Photo-Fenton; 300 W Xe lamp with 420 nm cutoff filter | Catalyst 125 mg/L; theophylline, ibuprofen 20 mg/L; almost complete degradation in 180 min; 40 mL $H_2O_2$/L; pH 4 | Potential of $Pd^{2+}/Pd^{0}$ (0.987 V vs. NHE) | [138] |

| | | | | | |
|---|---|---|---|---|---|
| MIL-101(Cr) | 1116-2561 $m^2/g$; pore diameter in two regions: < 2.5 nm and 3–4 nm | Photo-Fenton; 200 W halogen lamp 350–450 nm | Catalyst 100 mg/L; red X-3B dye, 100 mg/L; 94 % color and 60 % TOC removal in 120 min; 196 mM $H_2O_2$; pH 6 | XPS spectra for the oxidation states of Fe | [141] |
| MIL-88A(Fe)-Graphene Oxide | Up to 409 $m^2/g$; pore diameter 1.12/2.60-3.21 (for 9 wt% GO); band gap 2.19 eV | Photo-Fenton (500W Xe lamp 420 nm < λ < 760 nm) | Catalyst 400 mg/L; RhB 10 mg/L; pH 1-9; 80 min for complete removal or RhB (9 wt% GO) | Valence-band potential of MIL-88A(Fe)-Graphene Oxide = 1.49 V versus NHE; redox potential of RhB = 1.43 V vs. NHE | [143] |
| g-$C_3N_4$/$NH_2$-MIL-88B(Fe) | Lamellar nanosheets into spindle-shaped crystals; band gap of $NH_2$-MIL-88B(Fe) and g-$C_3N_4$ 1.14 and 2.70 eV | Photo-Fenton, 500W Xe lamp 420 nm cutoff filter | Catalyst 1 g/L; MB 30 mg/L; 100 % degradation in 120 min; 100 μL $H_2O_2$; pH 7 | VB of $NH_2$-MIL-88B(Fe) = 1.27 and g-$C_3N_4$ = 1.56 eV versus NHE; redox potential of OH−/OH (2.3 eV vs NHE) | [144] |
| $Cu_2O$/MIL(Fe/Cu) | 1553 $m^2/g$; band gap 1.3 eV | 500 W Xe lamp | Catalyst 500 mg/L; thiacloprid 80 mg/L; 82.3 % TOC removed in 80 min; $H_2O_2$ 49 mM | Redox potential of MIL(Fe) = 0.29 V; $Cu_2O$/MIL(Fe/Cu) = 0.2 V | [142] |
| MOF(Fe/Co)/Carbon aerogel | Optimal Fe:Co ratio 2:1 | Photo-electro-Fenton, 500 W Xe lamp | Working area 3 $cm^2$; distance between electrodes 2 cm; RhB or DMP 50 ppm in $Na_2SO_4$ (0.1 M); removal > 85 % in < 120 min; pH 3 | Flat-band potential of MOF(Fe/Co) = −0.64V versus SCE | [145] |

### 3.1.2. Sulfate radical-based advanced oxidation processes

Recently, AOP based on the generation of sulfate radicals ($SO_4^{\bullet-}$) received considerable attention. The main reason is that sulfate radicals have an oxidation power like hydroxyl radicals (standard redox potential 2.44 V to compare with 2.73 V for $HO^{\cdot}$) [146]. Besides, they have some advantages over hydroxyl-based AOP, which is mainly associated with the longer life of sulfate radicals in aqueous solution [147]. The practical applications of sulfate-based methods use PS or

PMS, which can be converted into sulfate radical by catalytic and non-catalytic processes. Heterogeneous systems based on transition metal oxides have demonstrated good performance for wastewater treatments based on the production of sulfate radicals [148, 149]. Several authors have investigated the production of sulfate radicals by iron-based MOF catalysis. $NH_2$-MIL-101(Fe) covalently modified with 2-anthraquinone sulfonate (AQS) showed redox activity upon PS activation for bisphenol A degradation. The catalytic performance of AQS-$NH_2$-MIL-101(Fe) was higher than $NH_2$-MIL-101(Fe) with 98% of bisphenol A removal after 2 h, as shown in Fig. 7(a), and rate constants one order of magnitude higher, which corresponded to an efficient electron-transfer mechanism [150]. MIL-53(Fe) was used as PS activator for the degradation of Acid Orange 7 using visible light LED irradiation, showing a high efficiency that was explained by the activation of PS by photogenerated electrons [151]. Several MIL(Fe) MOFs displayed good activity for the depletion of the probe dye Acid Orange 7 in an aqueous solution using a PS oxidation system. The results showed that the dominant radical species responsible for the degradation of the pollutant were $SO_4^{\cdot-}$ and $HO^{\cdot}$ with cage size influencing activity [152]. The proposed mechanism is explained in Fig. 7(b). First, pollutants become adsorbed on MOF surface, and after $S_2O_8^{2-}$ addition, $SO_4^{\cdot-}$ are generated by surface active sites of catalyst followed by $HO^{\cdot}$ and $O_2^{\cdot-}$ that lead to pollutant degradation. MIL-88A was used for Orange Gelb degradation upon PS activation, achieving removal > 95 % after 150 min, but the removal rate decreased after several cycles due to the loss of active sites [153]. Pu et al. used MIL-53(Fe) for PS activation showing increasing Fe(II)-CUS, the catalytic activity also increases. The authors suggested a mechanism based on heterogeneous PS activation running in parallel with homogeneous reaction in solution [154]. In most cases, a combination of $SO_4^{\cdot-}$ and $HO^{\cdot}$ radicals is acknowledged, and a combination of homogeneous and heterogeneous reactions is usually observed.

MIL-101(Fe) was also used as support for immobilizing different nanomaterials. Zhang et al. grafted ferrocene by the Schiff base reaction and used it as a catalyst for PMS activation [155]. The system was tested for the degradation of amaranth dye showing high activity attributed to a much lower activation energy. Sajjadi et al. created a nanocomposite by co-precipitation of $Fe_3O_4$ on Zn-based MOF-2 to serve as a catalyst to activate PS under US irradiation [156]. The catalyst was used for the degradation of the organophosphate insecticide diazinon with good activity and reusability. Fe(II)-MOF(1,4-BDC), a MOF with coordinatively unsaturated metal sites, was used to degrade dibutyl phthalate by PS activation. The data indicated that the activation process does not change the state of the central metal atom, being explained instead by the formation of an external electron transfer channel [157].

Several groups prepared non-Fe-based MOF for PS/PMS activation. Azhar et al. used a water-

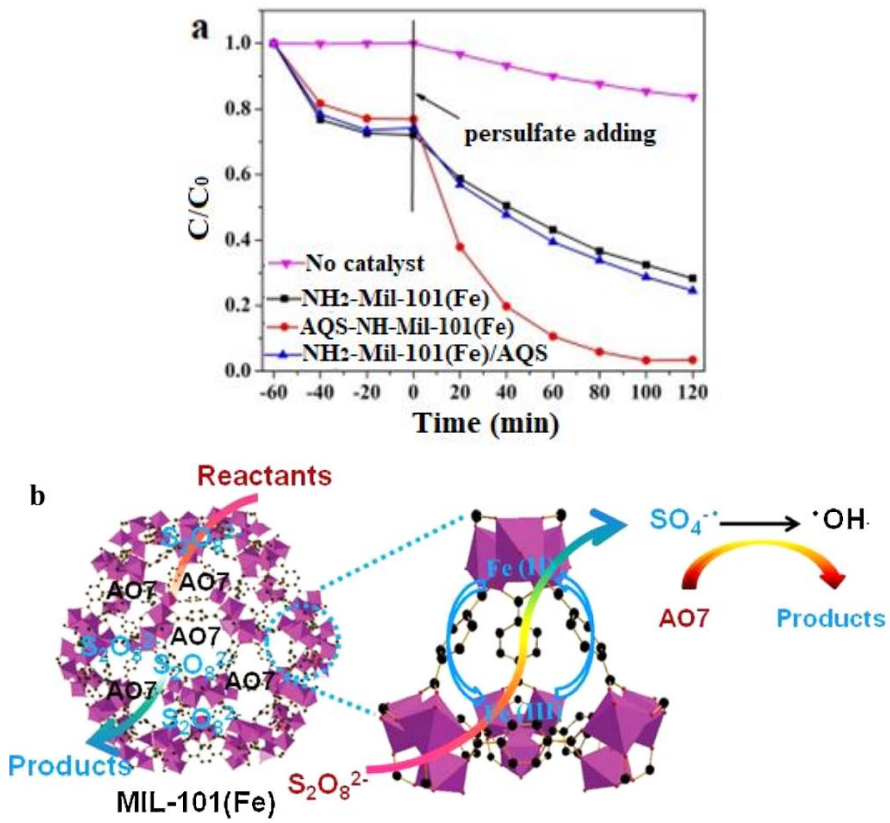


Fig. 7 (a) Removal performance of BPA in different catalytic conditions. Reproduced with permission from [150]. Copyright 2017 Elsevier. (b) Proposed mechanism for the degradation of Acid Orange 7 using MIL-101(Fe). Reprinted with permission from [152]. Copyright 2016 Elsevier.

stable Co-MOF, bio-MOF-11-Co, for PMS activation to catalytically degrade the broad-spectrum sulfonamide sullfachloropyridazine and p-hydroxybenzoic acid, a product of the hydrolysis of parabens, a group of substances widely used in cosmetic formulations [158]. Bio-MOF-11-Co showed rapid degradation of both sullfachloropyridazine and p-hydroxybenzoic acid with good reusability by water washing. Electronic paramagnetic resonance showed that both sulfate and hydroxyl radicals were responsible for degradation. The ligand adenine reinforced reaction kinetics by electron donation [158]. In another work, the Methyl Orange was degraded, using Co-MOF as a catalyst for PMS activation [159]. The redox-pair Co(II)/Co(III) in the Co-MOF initiated the $SO_3^{2-}$ oxidation, with the formation of oxysulfur radicals, mainly $SO_4^{\bullet-}$. The Co-MOF catalytically outperform homogenous Co(II) catalysts, Co nanoparticles embedded in carbon tubes and cobalt oxides of $Co_3O_4$ and $CoFe_2O_4$. The high performance was assigned to the special coordination of Co ions (Co(II) and Co(III)) and the ligand.

MOF-2, $Zn_2(BDC)_2$, nanomaterial was coupled with ultrasound (US) and PS activation for Acid Blue 7 degradation. The combined US/PS/MOF-2 outperformed US and US/PS alone

due to the action of the active species $HO^{\cdot}$, $SO_4^{\cdot-}$, $O_2^{\cdot-}$, $^1O_2^{\cdot}$ [160]. $Co_3(BTC)_2$ was used to activate PMS for the removal of DBP. However, degradation efficiency decreased from cycle to cycle due to the loss of active sites [161]. Li et. al used Cu-BTC to remove DBP in a wide pH range (2.0 – 10.0) and in the presence of PS [162]. However, the removal of DBP was not competed because the DBP was blocked outside due to its large molecular size. Yolk–shell $Co_3O_4$@MOF acted as a reactor for PMS activation with sulfate radicals being produced into its interior cavity. Mesoporous MOF shells direct reactants to encapsulated $Co_3O_4$ active sites allowing enhanced degradation of the organic compounds [163]. Pure sonocatalysis was studied by Nirumand et al. using magnetic MIL-101(Cr)/RGO/$ZnFe_2O_4$ composites and used it for the $H_2O_2$-assisted sonodegradation of organic dyes [164]. The composite catalyst outperformed pure MIL-101(Cr)/RGO, MIL-101(Cr) and $ZnFe_2O_4$, which was attributed to the generation of charge carriers in $ZnFe_2O_4$ and MIL-101(Cr) and their rapid separation and transfer to the surface of RGO. Trapping experiments showed that the main oxidizing agent are $HO^{\cdot}$. Repeated oxidation runs showed that the leaching of $Zn^{2+}$ and $Cr^{3+}$ was negligible after four cycles, indicating good stability [164]. A bimetallic MOFs of FeCo-MOF-74, based on divalent cations (Fe and Co), with high redox-active metal centers was able to activate PMS in order to achieve 100% degradation of phenanthrene (PHE) [165]. The coexistence of non-radical and radical species was due to the interaction of PMS and FeCo-MOF-74. Table 2 summarizes MOF catalysis in PS/PMS activation with the reaction conditions.

**Table 2.** MOFs in sulfate radical-based AOP for the removal of emerging aqueous pollutants

| MOFs | Characterization properties | Reaction | Reaction conditions | Redox properties/ potentials | Ref. |
|---|---|---|---|---|---|
| AQS-$NH_2$-MIL-101(Fe) [AQS = 2-anthraquinone sulfonate] | Octahedron smooth crystals 500–800 nm | PS activation | Catalyst 200 mg/L; bisphenol A, 60 mg/L; 98 % removal after 3 h; PS 10 mmol/L; pH 5.76 | Potetial of NH2-MIL-101(Fe)/ITO + 0.495 V; AQS-NH-MIL-101(Fe)/ITO = 0.44 V | [150] |
| Bio-MOF-11-Co (adenine) | Surface area 370 $m^2$/g. Pore size 3-5 nm and 10-15 nm | PS activation | Catalyst 50 mg/L; sullfachloropyridazine, p-hydroxybenzoic acid, 15–45 mg/L; generally complete removal in < 1 h; PMS 500 mg/L | Redox potential not given | [158] |

| | | | | | |
|---|---|---|---|---|---|
| MIL-101(Fe)<br>MIL-100(Fe)<br>MIL-53(Fe)<br>MIL-88B(Fe) | MIL-101(Fe) 32000-3400 $m^2/g$; MIL-100(Fe) 2400 $m^2/g$, MIL-53(Fe) 1000 $m^2/g$; MIL-88B(Fe) < 30 $m^2/g$; cage window from 12-16 Å in MIL-101(Fe) to 3 Å in MIL-88B(Fe) | PS activation | Catalyst 200 mg/L; Acid Orange 7; removal > 90 % for MIL-101(Fe); ~ 25 % for MIL-88B(Fe) | Electronic state of Fe measured by XPS analysis | [152] |
| Fe(II)-MOF(1,4-BDC) | Rod shape with chalk-like appearance and particle size about 10 μm length | PS activation | Catalyst 400 mg/L; dibutyl phthalate 5 mg/L; max. removal 86.7 %; PS/DBP molar ratio 30:1 to 350:1; pH 3-9 | Electronic state of Fe measured by XPS analysis | [157] |
| $Co_3(BTC)_2$ | Rod-like crystals with very small surface area (< 0.5 $m^2/g$) and pore volume | PMS activation | Catalyst 300 mg/L; DBP 5 mg/L; DBP degradation 100 % in 30 min; PMS 1.08 mM; pH 5-11 | Oxidation peaks at 0.13 V and 0.37 V | [161] |
| Ferrocene-MIL-101(Fe) | Surface area 580 $m^2/g$; mesoporous (pre diameter 10-100 nm) | PMS activation | Catalyst 200 mg/L; amaranth dye 50 mg/L; complete discoloration after 30 min; K-PMS 200 mg/L; pH 3-11 | XPS analysis to detect Fe(II)/Fe(III) | [155] |
| Yolk–shell $Co_3O_4$@MOF (Zn -Fe metallic precursors; $H_2BDC$ organic linkers) | 196 $m^2/g$; pore volume 0.41 $cm^3/g$ | PMS activation | Catalyst 500 mg/L; 4-chlorophenol 100 mg/L; 100 % removal in 60 min; PMS 0.8 mM; pH 7 | Quenching tests to identify the reactive oxidant | [163] |
| MIL-53(Fe) | 78-89 $m^2/g$; pore diameter 3-6 nm | PS activation | Catalyst 1 g/L; OG 90 mg/L; OG removal 98 % in 120 min; PS 32mM | XPS analysis detecting Fe(II)/Fe(III) | [154] |
| MIL-53(Fe) | | PS activation; visible light LED | Catalyst 600 mg/L; AO7, 17.5 mg/L; 100 % conversion after 90 | Band-gap energy 2.62 eV; redox potential of AO7 1.54 V | [151] |

| | | | | | |
|---|---|---|---|---|---|
| | | irradiation, 455 nm | min; PS 2.0 mM; initial pH 6.0 | | |
| MOF-2 [$Zn_2(BDC)_2$] | 943 $m^2/g$; pore diameter 1.9 nm | PS and US (36 kHz frequency and 150 W) | Catalyst 600 mg/L; Acid Blue 7 10 mg/L; > 90 % removal in 120 min; PS 6 mmol/L; pH 5 | Band-gap energy of $Zn_2(BDC)_2$ 3.92 eV | [160] |
| $Fe_3O_4$@MOF-2 | Spherical $Fe_3O_4$ nanoparticles on chalk-like 10 µm crystals of MOF-2 | PS and US (200 W/L) | Catalyst 700 mg/L; diazinon 30 mg/L; degradation > 95 %; 15 cycles without loss of activity; PS 10 mmol/L; pH 3 | Electronic state of Fe measured by XPS analysis | [156] |

### 3.1.3. Fanton-like and Sulfate radical-based Catalysts derived from MOF-templates

MOFs gained popularity in recent years as supramolecular templates to prepare hierarchical catalysts. The pyrolysis of certain MOF produced carbonaceous materials suitable for use in several Fenton-type and other AOP processes. Nano-ZVI@C-N fabricated from the calcination of Fe-based MOFs has been used as heterogeneous catalyst in electro-Fenton removal of the lipid regulator gemfibrozil from urban wastewater [166]. A flower-like Fenton FeCu@C catalyst was produced from the pyrolysis of iron-copper bimetallic MOF and applied to the removal of sulfamethazine in the presence of $H_2O_2$ [85]. The use of carbonaceous materials from the pyrolysis of MIL-100/dicyandiamide, with an organic linker containing N-precursor, was investigated by Liang et al., who produced N-doped graphene (N-C-Fe and N-G respectively before and after washing unstable iron species, Fig. 8a) [167]. Both materials were used for PMS activation and rapidly degraded several aqueous pollutants, including phenol and p-hydroxybenzoic acid. N-graphene (N-G) showed better catalytic activity, and the mechanism investigated by EPR and quenching tests showed that singlet oxygen ($^1O_2$) played the primary role. In contrast, the mechanisms for N-C-Fe proceeded via $HO^{\cdot}$. Co/Fe bimetallic MOF were used to prepare porous ferromagnetic cobalt ferrite ($CoFe_2O_4$) nanocrystals by calcination at 400 °C. The resulting $CoFe_2O_4$ was subsequently used to activate PMS for the degradation of bisphenol A. The catalytic activity was attributed to its surface area (60.4 $m^2/g$) and mesoporous structure. Significantly $Cl^-$ and $HCO_3^-/CO_3^{2-}$ improved degradation due to the production of reactive halogens and to the elevated solution pH [168]. Graphene-encapsulated metal nitrides ($Fe_xMn_{6-x}Co_4$–N@C) were produced by Li et al. decomposing MOF precursors at 650 °C in a

nitrogen atmosphere [169]. The precursors were Prussian blue analogues (PBA) ($Mn_yFe_{1-y}[Co(CN)_6]0.67 \cdot nH_2O$, $Mn_yFe_{1-y}$–Co PBAs; $0 < y < 1$) and the resulting catalysts tested for PMS activation to remove bisphenol A. The reaction proceeded by both sulfate and hydroxyl radicals, and catalytic performance improved by increased Mn content [169]. Cobalt oxides are well-known catalysts for PS/PMS activation. $Co_3O_4$-$Bi_2O_3$ composite prepared by calcination of a Bi-based MOF (Bi-BTC). The resulting material consisted of $Bi_2O_3$ rods decorated with $Co_3O_4$ nanoparticles. Again, the material was used for PMS-driven degradation of the azo dye RhB over a wide pH range [170]. The pyrolysis of Co, Zn-bimetallic zeolite imidazole frameworks on graphene oxide produced Fenton-like 2D porous carbon catalyst with Co/Co-$N_x$/pyridinic-N active sites in carbon nanotubes. The material was used for the degradation of several aqueous benzene-derived pollutants by PMS activation [171]. An aluminum-cobalt layered double hydroxide produced by etching of cobalt zeolitic imidazolate framework (Co-ZIF) was used as catalyst for tetracycline abatement by PMS activation [172]. Bimetallic Cu/Fe MOFs were used as template to produce copper ferrite by pyrolysis, which promoted sulfite autoxidation for the removal of the iodinated X-ray contrast iohexol. The performance of the catalysts in the presence of sulfite are represented in Fig. 8b. In this case, the mechanism proceeds via the formation of a surface Cu(II)–$SO_3^{2-}$ complex in which one electron transfer leads to $SO_3^{\cdot-}$, subsequently yielding $SO_4^{\cdot-}$ with dissolved oxygen [173]. The reported MOF-derived catalysts for these processes are concisely represented in Table 3.

**Table 3.** Fanton-like and sulfate radical-based catalysts derived from MOF-templates for the abatement of emerging pollutants

| Material | MOF precursor | Process and morphology | Reaction | Redox properties/ potentials | Ref. |
|---|---|---|---|---|---|
| FeCu@C | [Fe,Cu]-BDC | Pyrolysis at 600 °C in air; flower-like morphology with Fe-based 100-200 nm particles on carbonaceous sheets | Fenton-like catalyst (20 mg/L) for sulfamethoxazole 20 mg/L degradation; 1.5 mM $H_2O_2$; pH 3 | Redox potentials $Cu^{2+}/Cu^{+}$ (0.17 V) and $Fe^{3+}/Fe^{2+}$ (0.77 V) | [85] |
| Nano-ZVI@C-N (magnetic) | MIL(Fe)-88B<br>$NH_2$-MIL(Fe)-88B | Calcination 800 °C; core-shell nano-ZVI and $Fe_3O_4$ nanoparticles, 150−600 nm | Electro-Fenton (300 mA, cathode 3 $cm^2$) for the removal of gemfibrozil in 0.050 M $Na_2SO_4$ | Redox potential not given | [166] |

| | | | | | |
|---|---|---|---|---|---|
| N-doped graphene | MIL-100/dicyandiamide | 800 °C for 2 h in $N_2$ (N-C-Fe) and after washing with 0.5 M $H_2SO_4$ at 80 °C for 24 h (N-G) | PMS activation for degradation of phenol, 2,4,6-tricholophenol, sulfachloropyridazine and p-hydroxybenzoic acid (20-50 mg/L); catalyst 100 mg/L; PMS 3.25 mM | Quenching test to verify the active radicals | [167] |
| $CoFe_2O_4$ (ferromagnetic) | Co/Fe bimetallic MOF | Calcined for 1 h at 400 °C; rod-like particles 2-4 µm length | PMS activation; catalyst 100 mg/L; PMS 0.45 mM; BPA 10.3 mg/L; pH 6.5 | Redox potential CoII/CoIII 1.92 V; $Fe^{3+}/Fe^{2+}$ (0.77 V) | [168] |
| $Fe_xMn_{6-x}Co_4$–N@C | $Mn_yFe_{1-y}[Co(CN)_6]0.67 \cdot nH_2O$, $Mn_yFe_{1-y}$–Co PBAs; 0 < y < 1 | Thermal decomposition at 650 °C in $N_2$; nanodice 1-2 µm | PMS activation to remove BPA. Catalyst 100 mg/L; BPA 20 mg/L; PMS 0.2 g/L; pH 6.0. | XPS $Co^0$ & $Fe^0$ on the catalyst were oxidized during PMS activation | [169] |
| $Co_3O_4$-$Bi_2O_3$ | Bi-based MOF (Bi-BTC) | Calcination at 500 °C for 2 h; $Bi_2O_3$ rods decorated with $Co_3O_4$ nanoparticles | PMS activation for degrading azo dyes; catalyst 50 mg/L; PMS dosage 50 mg/L; RhB 10 mg/L | XPS to show the valence states of Co and Bi ions | [170] |
| Co/Co-$N_x$ co-doped N-CNT | Co, Zn-bimetallic ZIF (ZIF-67@ZIF-8) | Carbonization at 800 °C-1000 °C; CNT - encapsulated Co nanoparticles | PMS activation for degradation of BPA; catalyst 20 mg/L; BPA 20 mg/L; PMS 0.4 g/L; initial pH=6, | XPS revealed Co(0) and Co(II) species | [171] |
| AlCo-LDH | Co-ZIF | Co-ZIF in ethanol with $AlCl_3$ and US 400 W for 2 h; hexagonal sheets 3 × 1 µm x 180 nm | PMS activation for tetracycline abatement; catalyst 200 mg/L; tetracycline 30 mg/L; PMS 0.4 g/L | Via XPS: PMS activation by $Co^{2+}$; $Co^{2+}$ was oxidized to $Co^{3+}$ | [172] |
| Spinel $CuFe_2O_4$ | Bimetallic Cu/Fe MOFs | Calcination at 400 °C; rod-like structure | Sulfite autoxidation; catalyst 100 mg/L; Removal of iohexol, 8.2 mg/L; $Na_2SO_3$ 500 µM; time 30 min; pH 8.0. | Oxidation potential $Cl_2^{\bullet-}$ (2.09 V) < $SO_4^{\bullet-}$ (2.5–3.1 V); $Cl_2^{\bullet-}$ degradaed iohexol | [173] |

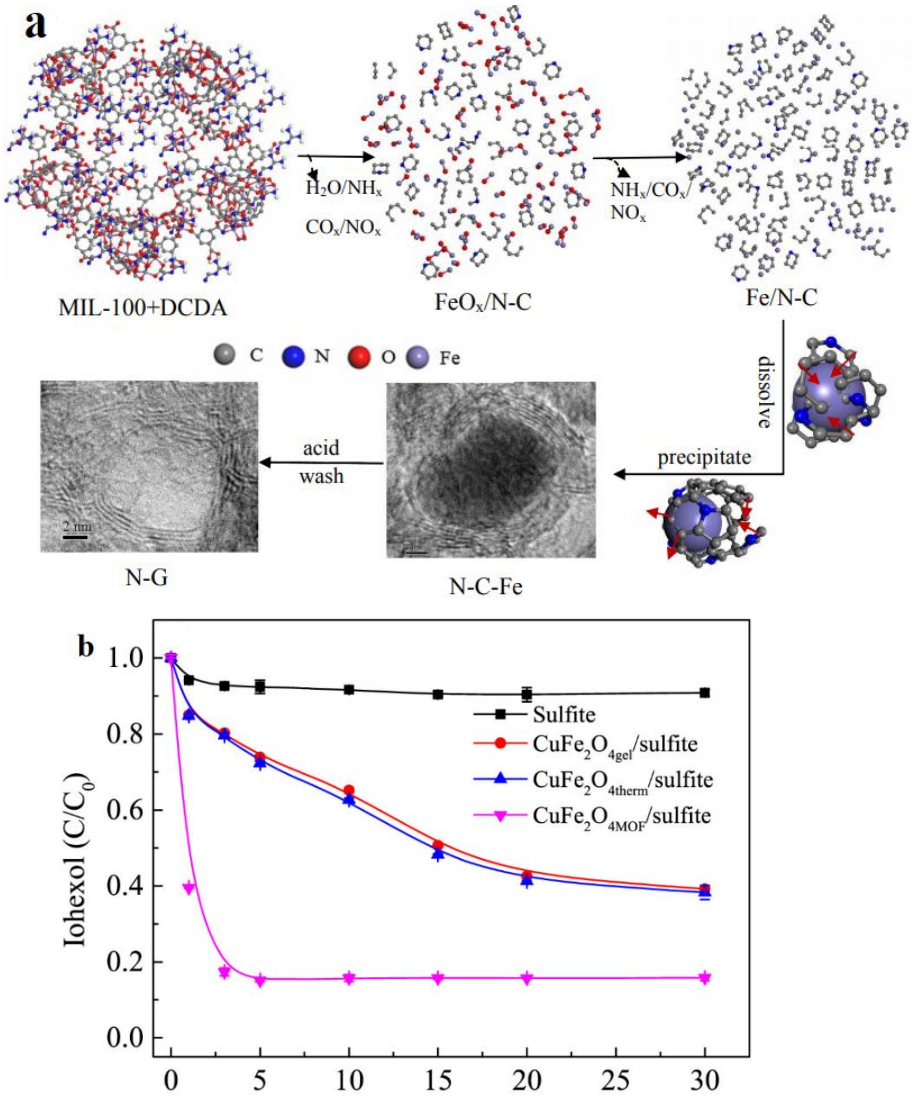


Fig. 8 (a) Production of N-C-Fe and N-G onion-like structures from MIL-100/dicyandiamide (DCDA). Reprinted with permission from [167]. Copyright 2017 The Royal Society of Chemistry. (b) The iohexol removal efficiency by sulfite in the presence of different bimetallic Cu/Fe MOFs. Reproduced with permission from [173]. Copyright 2020 Elsevier.

### 3.1.4. Photocatalysts for removing dissolved emerging pollutants

MOFs have attracted attention in photocatalysis due to their ordered porous structure, large surface area, and almost unlimited functionalization versatility. It is possible for MOFs to display semiconductor-like behavior in which metal-oxo clusters and organic linkers act as isolated quantum dots and light-absorbing antennas, respectively [174]. Contrary to conventional inorganic semiconductors, which

possess delocalized conduction and valence bands, MOFs are crystalline molecules in which light excited electrons can move from the HOMO to the LUMO. This mechanism is referred to as ligand-to-metal charge transfer [175]. Photogenerated electrons are eventually transferred to $O_2$ to produce superoxide radicals ($O_2^{\cdot-}$), while HOMO holes ($h^+$) may oxidize water to produce hydroxyl radicals ($HO^{\cdot}$) in the same way as inorganic semiconductors do. Also, like most semiconductors band gaps, many $E_{HOMO–LUMO}$ fall in the near-UV region. This is the case of UiO-66(Zr) or MIL-125(Ti), Fe-based MOF can be excited by visible light even though in many cases the degradation is slow and $H_2O_2$ is added as intermediate hydrogen acceptor to generate $HO^{\cdot}$ [176]. Following the established practice, we will use the term band gap for the transition energy.

There are several methods to create active MOF photocatalysts by increasing the absorption of light, especially in the visible range, or by facilitating the separation of charge carriers [177]. MOFs can be built using suitable ligands and metals or metal clusters using, for example, light-harvesting compounds. Strategies to reduce the recombination of photogenerated electrons and holes have led to composite material with heterojunctions or Schottky barriers. In the following paragraphs, we will present advances in using single-metal MOFs, nanoparticle composites and different MOF-semiconductor heterojunctions. Many MOFs have been tested for removing emerging compounds since the early use of MOF-5 to degrade phenol in an aqueous solution [178]. The application of MOF-based photocatalysis for environmental remediation has been recently reviewed [176, 179]. We summarize a selection of recent articles specifically dealing with the photocatalytic reduction of aqueous emerging pollutants, while photo-Fenton processes, proceeding with external addition of $H_2O_2$ and sometimes presented together with pure photocatalytic systems, were dealt with in the previous section.

Fe-MOFs with bandgap in the visible wavelength range, MIL-100(Fe) stands out due to its stability provided by the BTC linker. MIL-100(Fe) prepared in mild conditions was tested by Guesh et al. for the photocatalytic degradation of MO under ultraviolet and solar light radiation. The photocatalyst was reasonably active probably favored by its good textural properties [180]. Wang et al. tested several Fe-based MOFs (Fe-MIL-101, Fe-MIL-100, and Fe-MIL-53) for the degradation of the antibiotic tetracycline [181]. Trapping and ESR experiments showed that ESR tests indicated that $O_2^{\cdot-}$, $HO^{\cdot}$, and h+ were all involved in the oxidation processes of tetracycline. FeBTC modified with Amberlite IRA-200 showed improved stability and recyclability with lower recombination rate of photogenerated charge carrier [182]. Zn-based MOF $[Zn_2(odpt)(bpy)(H_2O)](bpy)_{0.5}$ ($H_4$odpt = 4,4′-oxidiphthalic acid, bpy = 4,4′-bipydine) has been checked for the photocatalytic degradation of the industrial dyes MB and MO. However, the bandgap for this material was 3.6 eV in the near-UV

wavelength and, therefore, little visible light activity was expected [183].

Metallic nanoparticles play a role in certain modifications of MOF-based photocatalysts. First, they act as electron acceptors due to their low Fermi level and the effect of localized surface plasmon resonance, which may enhance visible light absorption. Huang et al. [184] prepared Ag/AgCl@MIL-88A(Fe), a nanocomposite that benefits from plasmonic Ag/AgCl absorption with photocatalytic MOF for ibuprofen degradation. The authors showed visible light absorption enhancement in the < 600 nm wavelength and a higher photoinduced charge transfer rate. The mechanism explaining the photocatalytic activity of Ag/AgCl@MIL-88A(Fe) is shown in Fig. 9. MIL-88A(Fe) would produce photoinduced electrons/holes under visible light irradiation, while surface plasmon resonance would occur in metallic Ag nanoparticles. The electrons would move to CB of AgCl from Ag nanoparticles where $O_2^{\cdot-}$ would

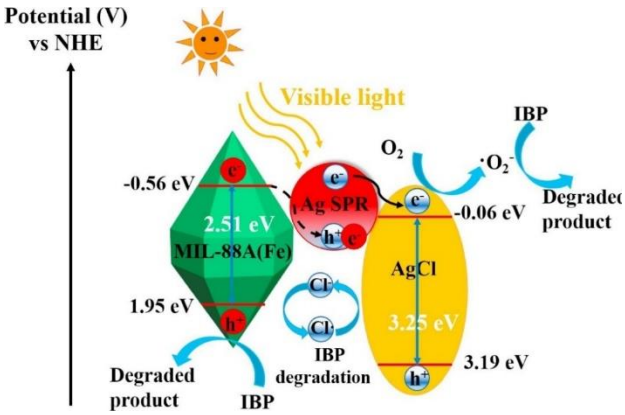


Fig. 9. Illustration of charge transfer in Ag/AgCl@MIL-88A(Fe) nanocomposite under visible light irradiation. Reproduced with permission from [184]. Copyright 2018 Elsevier.

be produced from $O_2$. Holes in Ag would recombine with photo-induced electrons from MIL-88A(Fe) and finally, the photo-holes in MIL-88A(Fe) would oxidize ibuprofen [184].

A GO/MIL-68(In)-$NH_2$ composite was used as a visible-light photocatalyst for the degradation of the broad-spectrum antibiotic amoxicillin. The activity of this hybrid material was attributed to the GO acting as electron transporters and as a sensitizer enhancing visible light absorption. $O_2^{\cdot-}$ and $h^+$ were deemed responsible for the photocatalytic mechanism. The CB potentials calculated from Mott-Schottky plots are −0.68 and −0.40 eV (vs. NHE) for MIL-68(In)-$NH_2$ and GO/MIL-68(In)-$NH_2$, respectively. VB potentials were 1.94 and 2.03 eV (vs. NHE), respectively, based on the bandgap values. A positive shift was observed in VB of GO/MIL-68(In)-$NH_2$, meaning higher oxidation capacity than MIL-68(In)-$NH_2$ [185].

A particularly productive field in recent years has been the creation of heterojunctions between MOFs and different semiconductors. $Bi_2MoO_6$ is one of the semiconductors that can be excited by visible light. UiO-66(Zr) is a MOF known for its high-water stability, resulting in good recyclability of UiO-66(Zr) composites. Ding et al. combined UiO-66(Zr) with $Bi_2MoO_6$ using electrostatic self-assembly and tested it for the visible light degradation of Rh B [186]. The purpose was to create a type II heterojunction to achieve efficient separation of photo-excited charges. The proposed mechanism is shown in Fig. 10. VB top and CB bottom of $Bi_2MoO_6$ correspond to 2.26 eV and

−0.19 eV vs. NHE; HOMO and LUMO positions for UiO-66(Zr) are about −0.09 eV and 3.56 eV vs. NHE. Therefore, electrons photogenerated in $Bi_2MoO_6$ can be transferred to UiO-66(Zr) LUMO (type II heterojunction) [186]. BiOBr, BiOI and AgI are other semiconductors incorporated to UiO-66 and other MOFs and used to degrade emerging compounds based on the same principle [187-190]. Similarly, Hu et al. used BiOCl/$NH_2$-MIL-125(Ti) for the industrial chemical ethylene glycol [191]. $BiVO_4$/MIL-125(Ti) were used to create a photocatalytic heterojunction applied to the visible light degradation of RhB explained by the transfer of photo-generated charges with activity explained by the formation of superoxide anion radicals and holes in $BiVO_4$ [192]. Recently, a disk-like shape $TiO_2$ derived from $NH_2$-MIL-125(Ti), was used to form a composite, $CdIn_2S_4$@$TiO_2$ which exhibited good performance for the degradation of malachite green. The $Ti^{3+}$ and $Ti^{4+}$ redox sites that are generated in the catalyst were mutually transformed in situ [193]. Guan et al. demonstrated that a flower-like $Fe_3O_4$@ZIF-67 composite could quickly degrade 70 % of CR under visible light irradiation [194]. The $Fe_3O_4$ was evenly dispersed on the surface of ZIF-67 and the predominant active species in the photocatalytic system are the superoxide radicals and holes.

Due to its low cost, water stability and band bap in the blue region of visible light (2.7 eV), graphitic carbon nitride (g-$C_3N_4$) constitutes an appealing photocatalyst to couple with photoactive MOFs in heterojunctions. Wang et al. prepared g-$C_3N_4$M/MIL-125(Ti) hybrids and tested them for the photocatalytic depletion of RhB under visible-light irradiation [195]. Up to 7.0 wt% -$C_3N_4$, there is an increase in visible-light absorption and benefit for charge transfer at the heterojunction. Photo-generated electrons from g-$C_3N_4$ migrate to $Ti^{4+}$ in the titanium–oxo cluster of MIL-125(Ti), where adsorbed oxygen form superoxide radicals favored by the strong reducing ability of $Ti^{3+}$ [195]. Similarly, a composite g-$C_3N_4$/MIL-100(Fe) were obtained via dip-coating that exhibited photocatalytic activity for the degradation RhB and MB under visible light [196]. Graphitic carbon nitride (g-$C_3N_4$) nanosheets were coupled with

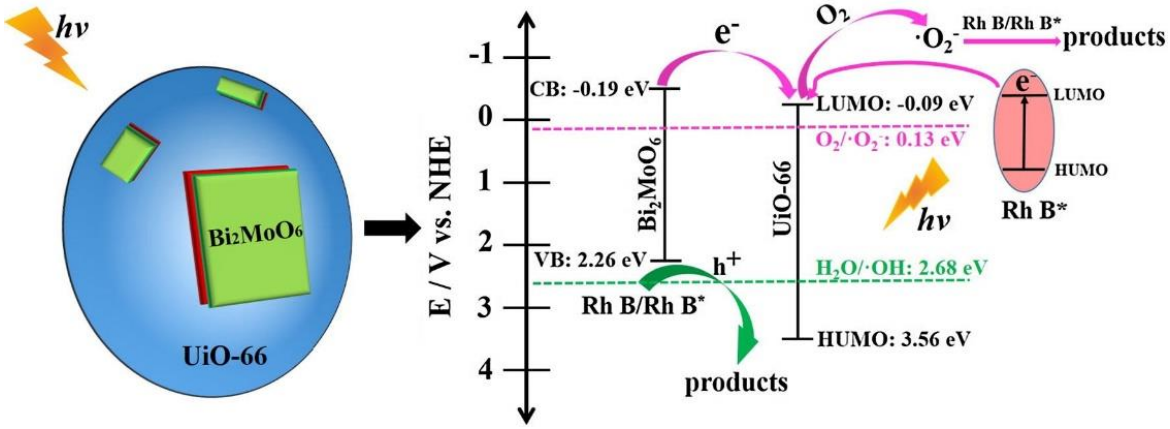

Fig. 10. Proposed removal mechanism for RhB on $Bi_2MoO_6$/UiO-66(Zr) heterojunction. Reprinted with permission from [186]. Copyright 2017 Elsevier.

UiO-66(Zr) using an annealing method to produce heterojunctions used for the photodegradation of MB under visible light irradiation. The results showed good photodegradation activity and stability (with 5 cycles without loss) for 50 % UiO-66/g-C3N4 hybrids attributed to the photoelectron transfer through the heterojunction from g-$C_3N_4$ CB to LUMO of UiO-66. As in other similar systems, trapping experiments revealed superoxide radicals ($O_2^{\cdot-}$) was the main oxidative species in the photodegradation with minor effect of holes in VB and hydroxyl radicals [197].

$In_2S_3$ is a photocatalyst with a band gap 2.0-2.4 eV. Wang et al. created a core-shell heterojunction combining it (shell) with MIL-125(Ti) (core) to provide efficient use of visible light irradiation [198]. The material has a mesoporous structure and visible-light absorption with good performance for the removal of tetracycline from water. The material is also a good adsorbent with a capacity reaching 157.2 mg/g due to surface complexation, π–π interactions, hydrogen bonding and electrostatic interactions. The photocatalytic performance was attributed to the transfer of photo-generated carriers to $Ti^{4+}$–$Ti^{3+}$ redox system. Remarkably, the material was tested with real wastewater matrixes, including medical wastewater, municipal wastewater and river water [198]. The same group prepared a heterojunction structure from $In_2S_3$ and UiO-66 and tested it for the photocatalytic removal of tetracycline. $In_2S_3$/UiO-66 displayed good adsorption capacity (> 100 mg/g). The trapping experiment and ESR measurements demonstrated that $O_2^{\cdot-}$ and holes explained the photocatalytic activity (Fig. 11). Under irradiation, the electrons move to CB of $In_2S_3$ and from there to LUMO of UiO-66 where they produce $O_2^{\cdot-}$, while the holes in the VB of $In_2S_3$ act as oxidation sites [199]. $AgIO_3$ is a novel semiconductor photocatalyst with a bandgap of 2.63 eV, which was assayed in

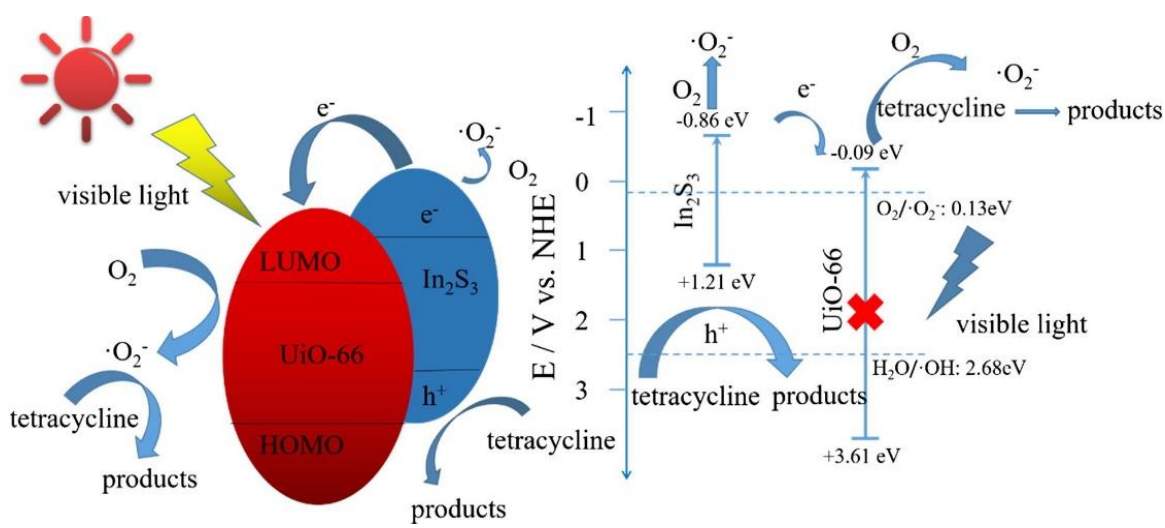

Fig. 11. Schematic illustration of the degradation mechanism of tetracycline over $In_2S_3$/UiO-66. Reproduced with permission from [199]. Copyright 2019 Elsevier.

composites with MIL-53(Fe) for the visible light decomposition of the organophosphorus pesticides, methyl malathion and chlorpyrifos. Again, the separation of photogenerated charges was assumed as the explanation for its activity [200]. Table 4 summarizes the photocatalytic MOFs and MOF composites applied for the removal of CECs.

**Table 4.** Photocatalytic applications of MOFs for removing dissolved emerging pollutants

| Material | Synthesis and main features | Band gap and irradiation | Redox properties/ potentials | Performance | Ref. |
|---|---|---|---|---|---|
| Amberlite IRA-200@FeBTC | Hydrothermal method and resin grafting; | Band gap 2.31 eV; 450 W Xe lamp with a 420 nm cutoff filter | Redox potentials RhB (1.3 V) & MB (1.08 V) < VB potential of FeBTC | Photocatalyst 270-530 mg/L; RhB 320 mg/L; 94 % degradation of 400 mg/L after 60 min; pH 7 | [182] |
| MIL-100(Fe) | Catalyst prepared using a simple method with $FeCl_2$ and $H_3BTC$; 1974 $m^2/g$; pore diameter 1.84 and 2.23 nm; stability not tested | Band gap 3.08 V; 150 W UV lamp and true solar irradiation for 6 h | Redox potential not given | Photocatalyst 0.33 mg/L; 5 mg/L MO; 64%; degraded under UV light (7 h); 40% under solar light irradiation (6 h outdoor experiment) | [180] |
| $Bi_2MoO_6$/UiO-66(Zr) | Electrostatic self-assembly of UiO-66(Zr) with $Bi_2MoO_6$; type II heterojunction; 209 $m^2/g$ for Bi:Zr ratio 2:1 | Band gap 3.64 eV; 500 W Xenon lamp with 420 nm cutoff filter | Potential of ($e^-$) is more nagative than ($O_2$/ $O_2^{\bullet-}$) (+0.13 eV) | Photocatalyst 500 mg/L; RhB 10 mg/L; 96 % removal in 120 mn; optimum Bi:Zr molar ratio 2:1; good stability and recyclability | [186] |
| g-$C_3N_4$M/MIL-125(Ti) | Solvothermal method, BDC linker; 328 $m^2/g$; av. pore diameter 6.8 nm | Band gap 3.24-3.50 eV; 300 W Xenon lamp, $\lambda > 420$ nm | Band potential g-$C_3N_4$ (+1.6 eV) more negative than redox potential ($OH/H_2O$) (+2.8). | Photocatalyst 160 mg/L; optimal g-$C_3N_4$ 7 wt%; RhB 40 mg/L | [195] |
| BiOBr/UiO-66 | Precipitation method; 149-486 $m^2/g$; good stability | Band gap 2.8-2.9 eV; 500 W halogen | Redox potential not given | Photocatalyst 500 mg/L; RhB 14.4 | [187] |

| | | | | | |
|---|---|---|---|---|---|
| | | lamp, 420 nm cutoff filter; irradiance 82 mW/cm$^2$ | | mg/L; completely degraded in 15 min | |
| AgI/UiO-66(Zr) | Solution method; stable after 4 cycles | Band gap 2.86 eV; 500 W halogen lamp, 420 nm cutoff filter; irradiance 82 mW/cm$^2$ | Quenching analysis confirmed $O_2^{\bullet-}$ as the active species RhB degradation | Photocatalyst 450 mg/L; RhB 14.4 mg/L; almost complete degradation in 60 min; higher activity Ag:Zr mol ratio 1:1 | [188] |
| g-$C_3N_4$/MIL-100(Fe) | g-$C_3N_4$ protonation and sol dip-coating of MIL-100(Fe); 1556 m$^2$/g; pore diameter 1.92 nm | Maximum absorption 405 nm; 300 W Xe lamp with cutoff filter | Redox potential not given; XPS showing Fe(III) oxidation state | Photocatalyst 1 g/L; RhB or MB 10 mg/L; > 85 % degradation in 200 min | [196] |
| g-$C_3N_4$/UiO-66(Zr) | Annealing at 350 °C for 2h in air; 384 m$^2$/g for 50 % hybrid; activity maintained after 5 cycles | Absorption edge at 480 nm; band gap 2.92 eV; 350 W Xe lamp with 420 nm cutoff filter | CB potential UiO-66 more negative than the reduction potential of $O_2$/ $O_2^{\bullet-}$ (−0.33 V) | Photocatalyst 250 mg/L; MB 10 mg/L; 100 % degradation in 24 min | [197] |
| $BiVO_4$/MIL-125(Ti) | Two-step hydrothermal synthesis; 80 % activity after 5 cycles | Band gap 2.25 eV; 500 W Xe lamp > 420 nm | Redox potential of $RhB^{+\bullet}$ (-1.42 eV) more nagative than $Ti^{4+/}Ti^{3+}$ (0.1 eV) | Photocatalyst 500 mg/L; RhB 10 mg/L; 92 % degradation in 180 min; best results for Bi:Ti molar ratio 3:2 | [192] |
| $In_2S_3$@MIL-125(Ti) | Solvothermal method; 209-304 m$^2$/g; pore diameter 3.7 nm | Band gap 2.28 eV; 300 W Xe lamp 420 nm cutoff filter | Redox potential not given | Photocatalyst 300 mg/L; tetracycline 64 mg/L; ~50 % removal in 60 min | [198] |
| $In_2S_3$/UiO-66 | Solvothermal method; best results for Zr:In molar ratio 0.37:1; 75 m$^2$/g | Band gap 1.92 eV (645 nm); 300 W Xenon lamp with a 420 nm cutoff filter | CB of $In_2S_3$ (−0.86 eV) < redox potential of ($O_2$/$O_2^{\bullet-}$) (+0.13 eV) | Photocatalyst 200 mg/L; tetracycline 40 mg/L; ~60 % removal in 60 min | [199] |
| Fe-MIL-101<br>Fe-MIL-100<br>Fe-MIL-53 | Syntheses by hydrothermal methods; 252 m$^2$/g(Fe-MIL-100), 1203 m$^2$/g (Fe- | Band gap 1.88 eV (Fe-MIL-101), 2.06 eV (Fe-MIL-100) and | Photogenerated electons from CB of Fe-MILs reduce $O_2$ to $^{\bullet}O_2^-$ | tetracycline 50 mg/L; removal 96.6% Fe-MIL-101, 57.4 % Fe- | [181] |

| | | | | | |
|---|---|---|---|---|---|
| | MIL-101), 21 $m^2/g$ (Fe-MIL-53) | 1.97 eV (Fe-MIL-53); 300 W Xenon lamp with 420 nm cutoff filter | | MIL-100, and 40.6 Fe-MIL-53 | |
| GO/MIL-68(In)-$NH_2$ | Synthesis by solvothermal method. Reused 3 times without loss of activity | Band gap 2.43 eV; 300 W Xenon lamp with 420 nm cutoff filter | CB of MIL-68(In)-$NH_2$/GrO (−0.40 eV) is more negative than $O_2$/ $^{\bullet}O_2^-$ (−0.046 eV vs. NHE) | Photocatalyst 600 mg/L; amoxicillin 20 mg/L; 93% removal after 120 min; 80 % TOC removal in 210 min; pH 5 | [185] |
| $AgIO_3$/MIL-53(Fe) | Ultrasonic synthesis; 208 $m^2/g$ | Band gap 2.63 eV; natural solar irradiation 600-730/$Wm^2$; | Redox potential not given | Photocatalyst 500 mg/L; methyl malathion and chlorpyrifos 5 mg/L; ∼78–90 % conversion in 60 min; 70 % mineralization in mixture after 180 min | [200] |
| Ag/AgCl@MIL-88A(Fe) | Solvothermal synthesis; 92-139 $m^2/g$; better results for Fe:Ag = 2:1; stable after 4 cycles | Band gap 2.51 eV; 500 W Xe lamp with 420 nm cutoff filter | CB of Ag/AgCl@MIL-88A(Fe) −0.75 V more negative than the redox potential of $O_2$/$^{\bullet}O_2^-$ (0.13 eV) | Photocatalyst 400 mg/L; ibuprofen 10 mg/L; > 90 % degradation and TOC removal in 3.5 h | [184] |

Besides pure photocatalysis, some combined processes have been studied for removing emerging pollutants from water. Co-doped MIL-53-$NH_2$ combined photocatalytic activity with PS activation and was tested for the degradation of several organic pollutants, including antibiotics and industrial dyes. The results proved that Co-doping reduced MIL-53-$NH_2$ bandgap, and $Co^{3+}/Co^{2+}$ redox system facilitated charge transfer suppressing the electron-hole recombination. The major contributors to the catalytic process were $SO_4^{\cdot-}$ and $HO^{\cdot}$ as expected from PS and h+ photocatalytic mechanisms [201]. In another example, Zhang et al. combined MIL-88A(Fe) photocatalysis with PS activation to degrade tetracycline using visible light irradiation [202]. In this case, ESR analysis also showed the involvement of $O_2^{\cdot-}$, besides $SO_4^{\cdot-}$, which would be produced from $O_2$ incompetence with $H_2O_2$ from photogenerated electrons in the CB of MIL-88A [202]. Finally, photocatalysts produced from the calcination of bimetallic Ni/Zn MOFs yield a $Ni_{0.9}Zn_{0.1}O$ phase, which lowers the band

gap of NiO and ZnO nanoparticles alone and that was successfully used for the degradation of MB. Trapping experiments showed that the predominant active species was photogenerated $HO^{\cdot}$[203].

## Conclusions and prospects

MOFs are evolving as an alternative to traditional porous materials to treat emerging contaminants due to their unique properties, particularly high porosity and surface area. Using the redox-active features of this hybrid material and incorporating them on appropriate substrate, future technological devices with efficient performance will be developed. Charge transfer within these three-dimensional coordination frameworks occurs via hopping or band transport regime, which can be promoted by engineering the metal cluster and/or organic linker, such as post-functionalization with electron-rich/deficient entities. Like the π–n and/or π–π* stacking interaction within the ligand enhances charge transfer. As inherent redox-active organic ligand and/or metal nodes are employed to construct MOFs, redox-active molecules can also be incorporated into the frameworks' cavities. Detailed understanding of the structure–function relationships will favor to prepare redox-active MOFs with the desired practical functionality. Thus, the principles of crystal engineering are very useful in designing and constructing redox-active MOFs. In addition, a high-performance redox-active MOFs will be achieved by rational balance of redox-active components incorporated in the frameworks. For practical application, it is important to integrate redox-active MOFs into suitable device architectures, thereby enhancing their overall CECs removal performance.

Water purification requires systems capable of simultaneously degrading many compounds in complex matrixes that include considerable amounts of natural organic matter. Designing multifunctional frameworks with active sites at both the nodes and the linker or at different components of the MOFs will be more desirable for this application. MOFs are effective adsorbents for emerging aqueous pollutants, and selective removal is favorable by tethering functional groups, like OH, $–NO_2$, and $–NH_2$, that improve the sorption capacity.

The prospect of redox-active MOFs for removing CECs is unprecedented, since the accessible redox-pairs can efficiently generate highly reactive strong oxidants, especially hydroxyl or sulfate radicals, that are capable of oxidizing several emerging pollutants, such as plasticizers (phthalates), pesticides (herbicides, insecticides), industrial chemicals (phenols, industrial dyes) and PPCPs (antibiotics, lipid regulators, anti-inflammatories). MOF-based photocatalysis display semiconductor-like behavior and light excited electrons usually move by ligand-to-metal charge transfer. Consequently, the superoxide radicals ($O_2^{\cdot-}$) and hydroxyl radicals ($HO^{\cdot}$) generated have been applied to remove emerging compounds. Results from photocatalytic runs are generally very basic. Information about fluence rate, emission models for lamps (two or three-dimensional, propagation in parallel planes or

spherical emission or extensive source models), local volumetric rate of photon absorption, or optical parameters are never given because no true photocatalytic reactors are used. Therefore, no scale-up or quantitative comparisons among results can be performed.

Cost-efficiency must be considered by developing simple and scalable synthesis methods and cost-effective procedures to regenerate active phases and recycle end-of-life materials. Therefore, unlike solvothermal synthesis, less energy-intensive preparation method of MOFs should be an area of more emphasis. In addition, some MOF materials are prepared from toxic organic moieties and metals, like 4,4-bipyridine and Cd, respectively, which can be released to the environment upon framework collapse.

Concerning applications in aqueous solution, there is a need to design sufficiently stable materials, capable of working under a wide range of pH conditions and in contact with highly oxidizing species. As instability is one of the main challenges of MOFs, therefore, chemical stability of these frameworks after using them for treating emerging pollutants should be considered and constructing stable MOFs is very important.

## Acknowledgement

C.I.E. acknowledge the financial support of the European Union Horizon 2020 research and innovation programme under the Marie Skłodowska-Curie grant agreement No 754382.

## Abbreviation

CECs = contaminants of emerging concern

PPCPs = pharmaceuticals and personal care products

EDCs = endocrine-disrupting compounds

MOFs = Metal-organic frameworks

PCN-222(Fe); PCN = porous coordination network

TCPP = tetrakis(4-carboxyphenyl)porphyrin

$[Zn(DMF))_2(TTFTC)(DPNI)]$ (DMF = N,N-dimethylformamide, TTFTC = tetrathiafulvalenetetracarboxylate, DPNI = N,N′-di-(4-pyridyl)-1,4,5,8-naphthalenetetracarboxydiimide

IVCT =intervalence charge transfer

$[Zn_2(BPPTzTz)_2(tdc)_2]$, (BPPTzTz = 2,5-bis(4-(pyridine-4-yl)phenyl)thiazolo[5,4-d]thiazole, tdc = 2,5-thiophene dicarboxylic acid

NIR = near infrared

SBUs = secondary building units

PSM = post-synthetic modification

$H_4$BTD-NDI = N,N′-bis(terphenyl-4,4″-di-carboxylic acid)naphthalenediimide

TTFTB = tetrathiafulvalene tetrabenzoate

HOMO = highest occupied molecular orbital

LUMO = lowest unoccupied molecular orbital

TTF = tetrathiafulvalene

NDIs = Naphthalenediimides

$H_4$NDISA = N,N′-bis(3-carboxy-4-hydroxyphenyl)-1,4,5,8-naphthalenetetradicarboximide

DPNDI = *N*,*N*′-di(4-pyridyl)-1,4,5,8-naphthalenetetra-carboxydiimide

TPA = triphenylamine

$H_3$TCA = 4,4′,4″-Tricarboxytriphenylamine

TCPP = tetrakis(4-carboxyphenyl)porphyrin

XANES = X-ray absorption near edge structure

XPS = X-ray photoelectron spectroscopy

TPrA = tripropylamine

bpy = 4,4′-bipydine

MIL-100(Fe); MIL = Materials of Institut Lavoisier

HKUST-1; HKUST = Hong Kong University of Science and Technology

fdc = furan-2,5-dicarboxylate

tdc = thiophene-2,5-dicarboxylate

CPO-27-$Ni^{II}$ ; CPO = Coordination polymer of Oslo

$^{t}BuSO_2PhIO$ = tert-butylsulfonyl-2-iodosylbenzene

HER = hydrogen evolution reactions

hfipbb = 4,4′-(hexafluoroisopropylidene)bisbenzoate

$H_3TCA$ = tricarboxytriphenyl amine

$H_2AQDC$=2,7-anthraquinonedicarboxylic acid

bdc = 1,4-benzenedicarboxylate

btb = 1,3,5-benzenetribenzoate

UiO-67; UiO = Universitetet i Oslo

NU-1000; NU = Northwestern University

AOP = Advanced oxidation processes

$HO^{\cdot}$ = hydroxyl radicals

PS = persulfate

PMS = peroxymonosulfate

Fe(II)-bpydc; bpydc = bipyridinedicarboxylate

PTA = phosphotungstic acid

AQS = 2-anthraquinone sulfonate

CUS = coordinatively unsaturated metal site

US = ultrasound

RGO = reduced graphene oxide

ZVI = zero-valent ion

PBA = Prussian blue analogues

ZIF = zeolitic imidazolate framework

NIE = normal hydrogen electrode

## References

[1] M. La Farre, S. Pérez, L. Kantiani, D. Barceló, Fate and toxicity of emerging pollutants, their metabolites and transformation products in the aquatic environment, Trends Anal. Chem. 27 (2008) 991-1007.

[2] T. Salthammer, Emerging indoor pollutants, Int. J. Hyg. Environ. Health. 224 (2020) 113423.

[3] Y. Zhou, J. Meng, M. Zhang, S. Chen, B. He, H. Zhao, Q. Li, S. Zhang, T. Wang, Which type of pollutants need to be controlled with priority in wastewater treatment plants: Traditional or emerging pollutants? Environ. Int. 131 (2019) 104982.

[4] K.O. K'oreje, M. Okoth, H. Van Langenhove, K. Demeestere, Occurrence and treatment of contaminants of emerging concern in the African aquatic environment: Literature review and a look ahead, J. Environ. Manage. 254 (2020) 109752.

[5] Y. Tang, Y. Zhong, H. Li, Y. Huang, X. Guo, F. Yang, Y. Wu, Contaminants of emerging concern in aquatic environment: Occurrence, monitoring, fate, and risk assessment, Water Environ. Res. 92 (2020) 1811-1817.

[6] R.M. Rego, G. Kuriya, M.D. Kurkuri, M. Kigga, MOF based engineered materials in water remediation: Recent trends, J. Hazard. Mater. 403 (2021) 123605.

[7] S. Rojas, P. Horcajada, Metal–organic frameworks for the removal of emerging organic contaminants in water, Chem. Rev. 120 (2020) 8378-8415.

[8] J. Zhu, S. Yuan, J. Wang, Y. Zhang, M. Tian, B. Van der Bruggen, Microporous organic polymer-based membranes or ultrafast molecular separations, Prog. Polym. Sci. (2020) 101308.

[9] C.I. Ezugwu, M.A. Asraf, X. Li, S. Liu, C.-M. Kao, S. Zhuiykov, F. Verpoort, Selective and adsorptive removal of anionic dyes and $CO_2$ with azolium-based metal-organic frameworks, J. Colloid Interface Sci. 519 (2018) 214-223.

[10] I. Ahmed, M.M.H. Mondol, H.J. Lee, S.H. Jhung, Application of Metal-organic frameworks in adsorptive removal of organic contaminants from water, fuel and air, Chem. Asian J. 16 (2021) 185-196.

[11] H. Vardhan, A. Mehta, C.I. Ezugwu, F. Verpoort, Self-assembled arene ruthenium metalla-assemblies, Polyhedron 112 (2016) 104-108.
[12] C.I. Ezugwu, B. Mousavi, M.A. Asrafa, A. Mehta, H. Vardhan, F. Verpoort, An N-heterocyclic carbene based MOF catalyst for Sonogashira cross-coupling reaction, Catal. Sci. Technol. 6 (2016) 2050-2054.
[13] W. Fan, X. Wang, B. Xu, Y. Wang, D. Liu, M. Zhang, Y. Shang, F. Dai, L. Zhang, D. Sun, Amino-functionalized MOFs with high physicochemical stability for efficient gas storage/separation, dye adsorption and catalytic performance, J. Mater. Chem. A. 6 (2018) 24486-24495.
[14] C.I. Ezugwu, S. Zhang, S. Li, S. Shi, C. Li, F. Verpoort, J. Yu, S. Liu, Efficient transformative HCHO capture by defective $NH_2$-UiO-66(Zr) at room temperature, Environ. Sci. Nano 6 (2019) 2931-2936.
[15] Y.-S. Wei, M. Zhang, R. Zou, Q. Xu, Metal–organic framework-based catalysts with single metal sites, Chem. Rev. 120 (2020) 12089-12174.
[16] B. Mousavi, S. Chaemchuen, C.I. Ezugwu, Y. Yuan, F. Verpoort, The effect of synthesis procedure on the catalytic performance of isostructural ZIF-8, Appl. Organomet. Chem. 32 (2018) e4062.
[17] I.A. Lazaro, R.S. Forgan, Application of zirconium MOFs in drug delivery and biomedicine, Chem. Commun. 380 (2019) 230-259.
[18] C.I. Ezugwu, M.A. Asraf, X. Li, S. Liu, C.-M. Kao, S. Zhuiykov, F. Verpoort, Cationic nickel metal-organic frameworks for adsorption of negatively charged dye molecules, Data Brief. 18 (2018) 1952-1961.
[19] D.M. D'Alessandro, Exploiting redox activity in metal–organic frameworks: concepts, trends and perspectives, Chem. Commun. 52 (2016) 8957-8971.
[20] N.L. Bazyakina, V.M. Makarov, S.Y. Ketkov, A.S. Bogomyakov, R.V. Rumyantcev, V.I. Ovcharenko, I.L. Fedushkin, Metal–organic frameworks derived from calcium and strontium complexes of a redox-active ligand, Inorg. Chem. 60 (2021) 3238-3248.
[21] M. Souto, J. Romero, J. Calbo, I.J. Vitórica-Yrezábal, J.L. Zafra, J. Casado, E. Ortí, A. Walsh, G. Mínguez Espallargas, Breathing-dependent redox activity in a tetrathiafulvalene-based metal–organic framework, J. Am. Chem. Soc. 140 (2018) 10562-10569.
[22] C. Wang, J. Kim, V. Malgras, J. Na, J. Lin, J. You, M. Zhang, J. Li, Y. Yamauchi, Metal–organic frameworks and their derived materials: Emerging catalysts for a sulfate radicals-based advanced oxidation process in water purification, Small 15 (2019) 1900744.
[23] D. Huang, G. Wang, M. Cheng, G. Zhang, S. Chen, Y. Liu, Z. Li, W. Xue, L. Lei, R. Xiao, Optimal preparation of catalytic Metal-organic framework derivatives and their efficient application in advanced oxidation processes, Chem. Eng. J. (2020) 127817.
[24] V.K. Sharma, M. Feng, Water depollution using metal-organic frameworks-catalyzed advanced oxidation processes: A review, J. Hazard. Mater. 372 (2019) 3-16.
[25] O. González, B. Bayarri, J. Aceña, S. Pérez, D. Barceló, Treatment technologies for wastewater reuse: Fate of contaminants of emerging concern, in: Advanced Treatment Technologies for Urban Wastewater Reuse, Springer, 2015, pp. 5-37.
[26] Y. Kurokawa, A. Maekawa, M. Takahashi, Y. Hayashi, Toxicity and carcinogenicity of potassium bromate--a new renal carcinogen, Environ. Health Perspect. 87 (1990) 309-335.
[27] L. Sun, M.G. Campbell, M. Dincă, Electrically conductive porous metal–organic frameworks, Angew.Chem. Int.Ed. 55 (2016) 3566-3579.
[28] J. Calbo, M.J. Golomb, A. Walsh, Redox-active metal–organic frameworks for energy conversion and storage, J. Mater. Chem. A 7 (2019) 16571-16597.
[29] C.-W. Kung, S. Goswami, I. Hod, T.C. Wang, J. Duan, O.K. Farha, J.T. Hupp, Charge transport in zirconium-based metal–organic frameworks, Acc. Chem. Res. 53 (2020) 1187-1195.
[30] G.S. Mohammad-Pour, K.O. Hatfield, D.C. Fairchild, K. Hernandez-Burgos, J. Rodríguez-López, F.J. Uribe-Romo, A solid-solution approach for redox active metal–organic frameworks with tunable redox conductivity, J. Am. Chem. Soc. 141 (2019) 19978-19982.

[31] N.F. Mott, Conduction in non-crystalline materials: III. Localized states in a pseudogap and near extremities of conduction and valence bands, Philos. Mag. 19 (1969) 835-852.

[32] K. Maindan, X. Li, J. Yu, P. Deria, Controlling charge-transport in metal–organic frameworks: contribution of topological and spin-state variation on the iron–porphyrin centered redox hopping rate, J. Phys. Chem. B 123 (2019) 8814-8822.

[33] C.F. Leong, P.M. Usov, D.M. D'Alessandro, Intrinsically conducting metal–organic frameworks, MRS Bull. 41 (2016) 858-864.

[34] L.S. Xie, G. Skorupskii, M. Dincă, Electrically conductive metal–organic frameworks, Chem. Rev. 120 (2020) 8536-8580.

[35] X. Deng, J.-Y. Hu, J. Luo, W.-M. Liao, J. He, Conductive metal–organic frameworks: mechanisms, design strategies and recent advances, Topics Curr. Chem. 378 (2020) 1-50.

[36] A.J. Clough, J.M. Skelton, C.A. Downes, A.A. De La Rosa, J.W. Yoo, A. Walsh, B.C. Melot, S.C. Marinescu, Metallic conductivity in a two-dimensional cobalt dithiolene metal–organic framework, J. Am. Chem. Soc. 139 (2017) 10863-10867.

[37] J.G. Park, M.L. Aubrey, J. Oktawiec, K. Chakarawet, L.E. Darago, F. Grandjean, G.J. Long, J.R. Long, Charge delocalization and bulk electronic conductivity in the mixed-valence metal–organic framework Fe(1,2,3-triazolate)$_2$($BF_4$)$_x$, J. Am. Chem. Soc. 140 (2018) 8526-8534.

[38] R. Murase, C.F. Leong, D.M. D'Alessandro, Mixed valency as a strategy for achieving charge delocalization in semiconducting and conducting framework materials, Inorg. Chem. 56 (2017) 14373–14382.

[39] M. Ko, L. Mendecki, K.A. Mirica, Conductive two-dimensional metal–organic frameworks as multifunctional materials, Chem. Commun. 54 (2018) 7873-7891.

[40] T. Neumann, J. Liu, T. Wächter, P. Friederich, F. Symalla, A. Welle, V. Mugnaini, V. Meded, M. Zharnikov, C. Wöll, Superexchange charge transport in loaded metal organic frameworks, ACS Nano 10 (2016) 7085-7093.

[41] A.A. Talin, A. Centrone, A.C. Ford, M.E. Foster, V. Stavila, P. Haney, R.A. Kinney, V. Szalai, F. El Gabaly, H.P. Yoon, Tunable electrical conductivity in metal-organic framework thin-film devices, Science 343 (2014) 66-69.

[42] S.S. Park, E.R. Hontz, L. Sun, C.H. Hendon, A. Walsh, T. Van Voorhis, M. Dincă, Cation-dependent intrinsic electrical conductivity in isostructural tetrathiafulvalene-based microporous metal–organic frameworks, J. Am. Chem. Soc. 137 (2015) 1774-1777.

[43] C. Leong, B. Chan, T. Faust, D. D'Alessandro, Controlling charge separation in a novel donor–acceptor metal–organic framework via redox modulation, 5 (2014) 4724-4728.

[44] C. Hua, P.W. Doheny, B. Ding, B. Chan, M. Yu, C.J. Kepert, D.M. D'Alessandro, Through-space intervalence charge transfer as a mechanism for charge delocalization in metal–organic frameworks, J. Am. Chem. Soc.140 (2018) 6622-6630.

[45] D. Shi, R. Zheng, M.J. Sun, X. Cao, C.X. Sun, C.J. Cui, C.S. Liu, J. Zhao, M. Du, Semiconductive Copper(I)–organic frameworks for efficient light-driven hydrogen generation without additional photosensitizers and cocatalysts, Angew. Chem. 129 (2017) 14829-14833.

[46] M.M. Deegan, T.S. Ahmed, G.P. Yap, E.D. Bloch, Structure and redox tuning of gas adsorption properties in calixarene-supported Fe (ii)-based porous cages, Chem. Sci. 11 (2020) 5273-5279.

[47] Y. Kamakura, S. Fujisawa, K. Takahashi, H. Toshima, Y. Nakatani, H. Yoshikawa, A. Saeki, K. Ogasawara, D. Tanaka, Redox-active tin metal–organic framework with a thiolate-based ligand, Inorg. Chem. 60 (2021) 12691-12695.

[48] C.I. Ezugwu, B. Mousavi, M.A. Asraf, Z. Luo, F. Verpoort, Post-synthetic modified MOF for Sonogashira cross-coupling and Knoevenagel condensation reactions, J. Catal. 344 (2016) 445-454.

[49] A. Mallick, H. Liang, O. Shekhah, J. Jia, G. Mouchaham, A. Shkurenko, Y. Belmabkhout, H.N. Alshareef, M. Eddaoudi, Made-to-order porous electrodes for supercapacitors: MOFs embedded with redox-active centers as a case study, Chem. Commun. 56 (2020) 1883-1886.

[50] Z. Yin, Q.-X. Wang, M.-H. Zeng, Iodine release and recovery, influence of polyiodide anions on electrical conductivity and nonlinear optical activity in an interdigitated and interpenetrated bipillared-bilayer metal–organic framework, J. Am. Chem. Soc. 134 (2012) 4857-4863.

[51] C.F. Leong, C.-H. Wang, C.D. Ling, D.M. D'Alessandro, A spectroscopic and electrochemical investigation of a tetrathiafulvalene series of metal–organic frameworks, Polyhedron 154 (2018) 334-342.

[52] B. Ding, M.B. Solomon, C.F. Leong, D.M. D'Alessandro, Redox-active ligands: Recent advances towards their incorporation into coordination polymers and metal-organic frameworks, Coord. Chem. Rev. 439 (2021) 213891.

[53] C.R. Wade, M. Li, M. Dincă, Facile deposition of multicolored electrochromic metal–organic framework thin films, Angew. Chem. Int. Ed. 52 (2013) 13377-13381.

[54] W. Liu, X.-B. Yin, Metal–organic frameworks for electrochemical applications, Trends Analyt. Chem. 75 (2016) 86-96.

[55] E.M. Miner, S. Gul, N.D. Ricke, E. Pastor, J. Yano, V.K. Yachandra, T. Van Voorhis, M. Dincă, Mechanistic evidence for ligand-centered electrocatalytic oxygen reduction with the conductive MOF $Ni_3$(hexaiminotriphenylene)$_2$, ACS Catal. 7 (2017) 7726-7731.

[56] H.-Y. Wang, L. Cui, J.-Z. Xie, C.F. Leong, D.M. D'Alessandro, J.-L. Zuo, Functional coordination polymers based on redox-active tetrathiafulvalene and its derivatives, Coord. Chem. Rev. 345 (2017) 342-361.

[57] J. Su, S. Yuan, H.-Y. Wang, L. Huang, J.-Y. Ge, E. Joseph, J. Qin, T. Cagin, J.-L. Zuo, H.-C. Zhou, Redox-switchable breathing behavior in tetrathiafulvalene-based metal–organic frameworks, Nat. Commun. 8 (2017) 1-8.

[58] H.Y. Wang, J.Y. Ge, C. Hua, C.Q. Jiao, Y. Wu, C.F. Leong, D.M. D'Alessandro, T. Liu, J.L. Zuo, Photo-and electronically switchable spin-crossover iron (ii) metal–organic frameworks based on a tetrathiafulvalene ligand, Angew. Chem. Int. Ed. 56 (2017) 5465-5470.

[59] J. Su, T.-H. Hu, R. Murase, H.-Y. Wang, D.M. D'Alessandro, M. Kurmoo, J.-L. Zuo, Redox Activities of Metal–organic frameworks incorporating rare-earth metal chains and tetrathiafulvalene linkers, Nat. Commun. 58 (2019) 3698-3706.

[60] F. Wang, J. Wang, S.F. Maehrlein, Y. Ma, F. Liu, X.-Y. Zhu, Broad-band near-infrared doublet emission in a tetrathiafulvalene-based metal–organic framework, J. Phys. Chem. Lett. 11 (2020) 762-766.

[61] Z.-N. Yin, Y.-H. Li, Y.-G. Sun, T. Chen, J. Xu, Q.-Y. Zhu, J. Dai, 3D copper tetrathiafulvalene redox-active network with 8-fold interpenetrating diamond-like topology, Inorg. Chem. 55 (2016) 9154-9157.

[62] P. Huo, T. Chen, J.-L. Hou, L. Yu, Q.-Y. Zhu, J. Dai, Ligand-to-ligand charge transfer within metal–organic frameworks based on manganese coordination polymers with tetrathiafulvalene-bicarboxylate and bipyridine ligands, Inorg. Chem. 55 (2016) 6496-6503.

[63] H.C. Wentz, M.G. Campbell, Fluoride detection with a redox-active naphthalene diimide metal–organic framework, 154 (2018) 309-313.

[64] K. AlKaabi, C.R. Wade, M. Dincă, Transparent-to-dark electrochromic behavior in naphthalene-diimide-based mesoporous MOF-74 analogs, Chem 1 (2016) 264-272.

[65] X. Kuang, S. Chen, L. Meng, J. Chen, X. Wu, G. Zhang, G. Zhong, T. Hu, Y. Li, C.-Z. Lu, Supramolecular aggregation of a redox-active copper-naphthalenediimide network with intrinsic electron conduction, Chem. Commun. 55 (2019) 1643-1646.

[66] B. Tan, C. Chen, L.-X. Cai, Y.-J. Zhang, X.-Y. Huang, J. Zhang, Introduction of lewis acidic and redox-active sites into a porous framework for ammonia capture with visual color response, Inorg. Chem. 54 (2015) 3456-3461.

[67] Z.-P. Dong, J.-J. Zhao, P.-Y. Liu, Z.-L. Liu, Y.-Q. Wang, A metal–organic framework constructed by a viologen-derived ligand: photochromism and discernible detection of volatile amine vapors, New J. Chem. 43 (2019) 9032-9038.

[68] H.-Y. Li, H. Xu, S.-Q. Zang, T.C. Mak, A viologen-functionalized chiral Eu-MOF as a

platform for multifunctional switchable material, Chem. Commun. 52 (2016) 525-528.
[69] H. Wu, M. Li, Z. Wang, H. Yu, J. Han, G. Xie, S. Chen, Highly stable Ni-MOF comprising triphenylamine moieties as a high-performance redox indicator for sensitive aptasensor construction, Anal. Chim. Acta. 1049 (2019) 74-81.
[70] J. Liu, X.Y. Daphne Ma, Z. Wang, L. Xu, T. Xu, C. He, F. Wang, X. Lu, Highly stable and rapid switching electrochromic thin films based on metal–organic frameworks with redox-active triphenylamine ligands, ACS Appl. Mater. Interfaces 12 (2020) 7442-7450.
[71] F. Leng, H. Liu, M. Ding, Q.-P. Lin, H.-L. Jiang, Boosting photocatalytic hydrogen production of porphyrinic MOFs: the metal location in metalloporphyrin matters, ACS Catal. 8 (2018) 4583-4590.
[72] E.X. Chen, M. Qiu, Y.F. Zhang, Y.S. Zhu, L.Y. Liu, Y.Y. Sun, X. Bu, J. Zhang, Q. Lin, Acid and base resistant zirconium polyphenolate-metalloporphyrin scaffolds for efficient $CO_2$ photoreduction, Adv. Mater. 30 (2018) 1704388.
[73] T. Pila, P. Chirawatkul, P. Piyakeeratikul, V. Somjit, M. Sawangphruk, K. Kongpatpanich, Metalloporphyrin-based metal–organic frameworks on flexible carbon paper for electrocatalytic nitrite oxidation, Chem. Eur. J. 26 (2020) 17399-17404.
[74] S.R. Ahrenholtz, C.C. Epley, A.J. Morris, Solvothermal preparation of an electrocatalytic metalloporphyrin MOF thin film and its redox hopping charge-transfer mechanism, J. Am. Chem. Soc. 136 (2014) 2464-2472.
[75] E.M. Johnson, R. Haiges, S.C. Marinescu, Covalent-organic frameworks composed of rhenium bipyridine and metal porphyrins: Designing heterobimetallic frameworks with two distinct metal sites, ACS Appl. Mater. Interfaces. 10 (2018) 37919-37927.
[76] P. Gayathri, K. Ramanujam, Redox active cobalt-bipyridine metal organic framework-nafion coated carbon nanotubes for sensing ascorbic acid, J. Electrochem. Soc. 165 (2018) B603.
[77] S.J. Stoneburner, L. Gagliardi, Air separation by catechol-ligated transition metals: a quantum chemical screening, J. Phys. Chem. C, 122 (2018) 22345-22351.
[78] S.J. Stoneburner, H. Demir, W. Jeong, D. Ray, X. Zhang, O.K. Farha, C.J. Cramer, I. Siepmann, L. Gagliardi, Metal-organic frameworks with metal catecholates for $O_2/N_2$ separation, J. Phys. Chem. C 123 (2019) 12935-12946.
[79] Y. Xu, X.-B. Yin, X.-W. He, Y.-K. Zhang, Electrochemistry and electrochemiluminescence from a redox-active metal-organic framework, Biosens. Bioelectron. 68 (2015) 197-203.
[80] Y. Zhang, S.N. Riduan, J. Wang, Redox active metal-and covalent organic frameworks for energy storage: Balancing porosity and electrical conductivity, Chem. Eur. J. 23 (2017) 16419-16431.
[81] A.-R. Kim, T.-U. Yoon, E.-J. Kim, J.W. Yoon, S.-Y. Kim, J.W. Yoon, Y.K. Hwang, J.-S. Chang, Y.-S.J.C.E.J. Bae, Facile loading of Cu(I) in MIL-100(Fe) through redox-active Fe(II) sites and remarkable propylene/propane separation performance, Chem. Eng. J. 331 (2018) 777-784.
[82] A.S. Duke, E.A. Dolgopolova, R.P. Galhenage, S.C. Ammal, A. Heyden, M.D. Smith, D.A. Chen, N.B. Shustova, Active sites in copper-based metal–organic frameworks: Understanding substrate dynamics, redox processes, and valence-band structure, J. Phys. Chem. C 119 (2015) 27457-27466.
[83] Y. Kim, K. Kim, H.H. Eom, X. Su, J.W. Lee, Electrochemically-assisted removal of cadmium ions by redox active Cu-based metal-organic framework, Chem. Eng. J 421 (2021) 129765.
[84] Y.M. Litvinova, Y.M. Gayfulin, K.A. Kovalenko, D.G. Samsonenko, J. Van Leusen, I.V. Korolkov, V.P. Fedin, Y.V. Mironov, Multifunctional metal–organic frameworks based on redox-active rhenium octahedral clusters, Inorg. Chem. 57 (2018) 2072-2084.
[85] J. Tang, J. Wang, MOF-derived three-dimensional flower-like FeCu@C composite as an efficient Fenton-like catalyst for sulfamethazine degradation, Chem. Eng. J. 375 (2019) 122007.
[86] N.S. Lopa, M.M. Rahman, F. Ahmed, S.C. Sutradhar, T. Ryu, W.J. Kim, A Ni-based redox-active metal-organic framework for

sensitive and non-enzymatic detection of glucose, J. Electroanal. Chem. 822 (2018) 43-49.

[87] J. Canivet, A. Fateeva, Y. Guo, B. Coasne, D. Farrusseng, Water adsorption in MOFs: fundamentals and applications, Chem. Sci. 43 (2014) 5594-5617.

[88] A.W. Stubbs, L. Braglia, E. Borfecchia, R.J. Meyer, Y. Román-Leshkov, C. Lamberti, M. Dincă, Selective catalytic olefin epoxidation with MnII-exchanged MOF-5, ACS Catal. 8 (2018) 596-601.

[89] C.K. Brozek, J.T. Miller, S.A. Stoian, M. Dincă, NO disproportionation at a mononuclear site-isolated $Fe^{2+}$ center in $Fe^{2+}$-MOF-5, J. Am. Chem. Soc. 137 (2015) 7495-7501.

[90] V. Khrizanforova, R. Shekurov, V. Miluykov, M. Khrizanforov, V. Bon, S. Kaskel, A. Gubaidullin, O. Sinyashin, Y. Budnikova, 3D Ni and Co redox-active metal–organic frameworks based on ferrocenyl diphosphinate and 4, 4′-bipyridine ligands as efficient electrocatalysts for the hydrogen evolution reaction, Dalton Trans. 49 (2020) 2794-2802.

[91] M.K. Leszczyński, A. Kornowicz, D. Prochowicz, I. Justyniak, K. Noworyta, J. Lewiński, Straightforward synthesis of single-crystalline and redox-active Cr(II)-carboxylate MOFs, Inorg. Chem. 57 (2018) 4803-4806.

[92] Z. Peng, X. Yi, Z. Liu, J. Shang, D. Wang, Triphenylamine-based metal–organic frameworks as cathode materials in lithium-ion batteries with coexistence of redox active sites, high working voltage, and high rate stability, ACS Appl. Mater. Interfaces 8 (2016) 14578-14585.

[93] Z. Zhang, H. Yoshikawa, K. Awaga, Monitoring the solid-state electrochemistry of Cu(2, 7-AQDC)(AQDC= anthraquinone dicarboxylate) in a lithium battery: Coexistence of metal and ligand redox activities in a metal–organic framework, J. Am. Chem. Soc. 136 (2014) 16112-16115.

[94] Q. Chen, J. Sun, P. Li, I. Hod, P.Z. Moghadam, Z.S. Kean, R.Q. Snurr, J.T. Hupp, O.K. Farha, J.F. Stoddart, A redox-active bistable molecular switch mounted inside a metal–organic framework, J. Am. Chem. Soc. 138 (2016) 14242-14245.

[95] S. Liu, J. Xu, E. Dai, J. Qiu, Y. Liu, Synthesis and properties of ferrocene confined within UiO-67 MOFs, Microporous Mesoporous Mater. 264 (2018) 133-138.

[96] J.E. Halls, C.Y. Cummings, J. Ellis, L.L. Keenan, D. Jiang, A.D. Burrows, F. Marken, Redox reactivity of methylene blue bound in pores of umcm-1 metal-organic frameworks, Mol. Cryst. Liq. Cryst. 554 (2012) 12-21.

[97] X. Liao, F. Wang, F. Wang, Y. Cai, Y. Yao, B.-T. Teng, Q. Hao, L. Shuxiang, Synthesis of (100) surface oriented MIL-88A-Fe with rod-like structure and its enhanced fenton-like performance for phenol removal, Appl. Catal. B 259 (2019) 118064.

[98] C. Zhang, S. Tian, F. Qin, Y. Yu, D. Huang, A. Duan, C. Zhou, Y. Yang, W. Wang, Y. Zhou, Catalyst-free activation of permanganate under visible light irradiation for sulfamethazine degradation: Experiments and theoretical calculation, Water Res. 194 (2021) 116915.

[99] L. Rizzo, S. Malato, D. Antakyali, V.G. Beretsou, M.B. Đolić, W. Gernjak, E. Heath, I. Ivancev-Tumbas, P. Karaolia, A.R. Lado Ribeiro, G. Mascolo, C.S. McArdell, H. Schaar, A.M.T. Silva, D. Fatta-Kassinos, Consolidated vs new advanced treatment methods for the removal of contaminants of emerging concern from urban wastewater, Sci. Total Environ. 655 (2019) 986-1008.

[100] B.N. Bhadra, D.K. Yoo, S.H. Jhung, Carbon-derived from metal-organic framework MOF-74: A remarkable adsorbent to remove a wide range of contaminants of emerging concern from water, Appl. Surf. Sci. 504 (2020) 144348.

[101] A.G. Slater, A.I. Cooper, Function-led design of new porous materials, Science 348 (2015) aaa8075.

[102] L. Jiao, J.Y.R. Seow, W.S. Skinner, Z.U. Wang, H.-L. Jiang, Metal–organic frameworks: Structures and functional applications, Mater. Today 27 (2019) 43-68.

[103] S. Dhaka, R. Kumar, A. Deep, M.B. Kurade, S.-W. Ji, B.-H. Jeon, Metal–organic frameworks (MOFs) for the removal of emerging contaminants from aquatic

environments, Coord. Chem. Rev. 380 (2019) 330-352.
[104] Z. Hasan, S.H. Jhung, Removal of hazardous organics from water using metal-organic frameworks (MOFs): plausible mechanisms for selective adsorptions, J. Hazard. Mater. 283 (2015) 329-339.
[105] W. Liu, X. Shen, Y. Han, Z. Liu, W. Dai, A. Dutta, A. Kumar, J. Liu, Selective adsorption and removal of drug contaminants by using an extremely stable Cu(II)-based 3D metal-organic framework, Chemosphere 215 (2019) 524-531.
[106] D. Sompornpailin, C. Ratanatawanate, C. Sattayanon, S. Namuangruk, P. Punyapalakul, Selective adsorption mechanisms of pharmaceuticals on benzene-1,4-dicarboxylic acid-based MOFs: Effects of a flexible framework, adsorptive interactions and the DFT study, Sci. Total Environ. 720 (2020) 137449.
[107] S. Lin, Y. Zhao, Y.-S. Yun, Highly effective removal of nonsteroidal anti-inflammatory pharmaceuticals from water by Zr(IV)-based metal–organic framework: adsorption performance and mechanisms, ACS Appl. Mater. Interfaces 10 (2018) 28076-28085.
[108] P. Zhao, N. Liu, C. Jin, H. Chen, Z. Zhang, L. Zhao, P. Cheng, Y. Chen, UiO-66: An advanced platform for investigating the influence of functionalization in the adsorption removal of pharmaceutical waste, Inorg. Chem. 58 (2019) 8787-8792.
[109] P.W. Seo, B.N. Bhadra, I. Ahmed, N.A. Khan, S.H. Jhung, Adsorptive removal of pharmaceuticals and personal care products from water with functionalized metal-organic frameworks: Remarkable adsorbents with hydrogen-bonding abilities, Sci. Rep. 6 (2016) 34462.
[110] J.Y. Song, S.H. Jhung, Adsorption of pharmaceuticals and personal care products over metal-organic frameworks functionalized with hydroxyl groups: Quantitative analyses of H-bonding in adsorption, Chem. Eng. J. 322 (2017) 366-374.
[111] P.W. Seo, N.A. Khan, S.H. Jhung, Removal of nitroimidazole antibiotics from water by adsorption over metal–organic frameworks modified with urea or melamine, Chem. Eng. J. 315 (2017) 92-100.
[112] B.N. Bhadra, S.H. Jhung, Adsorptive removal of wide range of pharmaceuticals and personal care products from water using bio-MOF-1 derived porous carbon, Microporous Mesoporous Mater. 270 (2018) 102-108.
[113] H.J. An, B.N. Bhadra, N.A. Khan, S.H. Jhung, Adsorptive removal of wide range of pharmaceutical and personal care products from water by using metal azolate framework-6-derived porous carbon, Chem. Eng. J. 343 (2018) 447-454.
[114] N. Zhuo, Y. Lan, W. Yang, Z. Yang, X. Li, X. Zhou, Y. Liu, J. Shen, X. Zhang, Adsorption of three selected pharmaceuticals and personal care products (PPCPs) onto MIL-101(Cr)/natural polymer composite beads, Sep. Purif. Technol. 177 (2017) 272-280.
[115] L. Sruthi, B. Janani, S.S. Khan, Ibuprofen removal from aqueous solution via light-harvesting photocatalysis by nano-heterojunctions: A review, Sep. Purif. Technol. (2021) 119709.
[116] S. Naeimi, H. Faghihian, Application of novel metal organic framework, MIL-53(Fe) and its magnetic hybrid: For removal of pharmaceutical pollutant, doxycycline from aqueous solutions, Environ. Toxicol. Pharmacol. 53 (2017) 121-132.
[117] S. Naeimi, H. Faghihian, Remediation of pharmaceutical contaminated water by use of magnetic functionalized metal organic framework. Physicochemical study of doxycycline adsorption, Water Environ J. 32 (2018) 422-432.
[118] Y. Yin, M. Shi, Y. Ren, S. Wang, M. Hua, J. Lu, W. Zhang, L. Lv, Wrinkle structure on multifunctional MOFs to facilitate PPCPs adsorption in wastewater, Chem. Eng. J. 387 (2020) 124196.
[119] D.B. Miklos, C. Remy, M. Jekel, K.G. Linden, J.E. Drewes, U. Hübner, Evaluation of advanced oxidation processes for water and wastewater treatment – A critical review, Water Res. 139 (2018) 118-131.
[120] J. Collins, J.R. Bolton, Advanced Oxidation Handbook, American Water Works Association, Denver, CO, 2016.
[121] K.-Y. Park, S.-Y. Choi, S.-H. Lee, J.-H. Kweon, J.-H. Song, Comparison of formation of disinfection by-products by chlorination and ozonation of wastewater effluents and

their toxicity to *Daphnia magna*, Environ. Pollut. 215 (2016) 314-321.

[122] F. Sun, H. Liu, H. Wang, D. Shu, T. Chen, X. Zou, F. Huang, D. Chen, A novel discovery of a heterogeneous Fenton-like system based on natural siderite: A wide range of pH values from 3 to 9, Sci. Total Environ. 698 (2020) 134293.

[123] P.V. Nidheesh, Heterogeneous Fenton catalysts for the abatement of organic pollutants from aqueous solution: a review, RSC Adv. 5 (2015) 40552-40577.

[124] C.I. Ezugwu, O.T. Ujam, P.O. Ukoha, N.N. Ukwueze, Complex formation and extraction studies of N, N¢-Bis (salicylidene)-3, 5-diaminobenzoic acid on Hg(II) and Ag(I), Chem. Sci. Trans. 2 (2013) 1118-1125.

[125] D. Wu, J. Jiang, N. Tian, M. Wang, J. Huang, D. Yu, M. Wu, H. Ni, P. Ye, Highly efficient heterogeneous photo-Fenton BiOCl/MIL-100 (Fe) nanoscaled hybrid catalysts prepared by green one-step coprecipitation for degradation of organic contaminants, RSC Adv. 11 (2021) 32383-32393.

[126] X. Zhang, N. Yuan, Y. Li, L. Han, Q. Wang, Fabrication of new MIL-53(Fe)@$TiO_2$ visible-light responsive adsorptive photocatalysts for efficient elimination of tetracycline, Chem. Eng. J. 428 (2022) 131077.

[127] S. Zhang, Y. Zhuo, C.I. Ezugwu, C.-c. Wang, C. Li, S. Liu, Synergetic molecular oxygen activation and catalytic oxidation of formaldehyde over defective MIL-88B(Fe) nanorods at room temperature, Environ. Sci. Technol. 55 (2021) 8341–8350.

[128] Q. Sun, M. Liu, K. Li, Y. Han, Y. Zuo, F. Chai, C. Song, G. Zhang, X. Guo, Synthesis of Fe/M (M = Mn, Co, Ni) bimetallic metal organic frameworks and their catalytic activity for phenol degradation under mild conditions, Inorg. Chem. Front. 4 (2017) 144-153.

[129] F.-X. Wang, C.-C. Wang, X. Du, Y. Li, F. Wang, P. Wang, Efficient removal of emerging organic contaminants via photo-Fenton process over micron-sized Fe-MOF sheet, Chem. Eng. J. (2021) 132495.

[130] H. Lv, H. Zhao, T. Cao, L. Qian, Y. Wang, G. Zhao, Efficient degradation of high concentration azo-dye wastewater by heterogeneous Fenton process with iron-based metal-organic framework, J. Mol. Catal. A: Chem. 400 (2015) 81-89.

[131] C. Zhou, L. Zhu, L. Deng, H. Zhang, H. Zeng, Z. Shi, Efficient activation of peroxymonosulfate on CuS@MIL-101(Fe) spheres featured with abundant sulfur vacancies for coumarin degradation: Performance and mechanisms, Sep. Purif. Technol. 276 (2021) 119404.

[132] Q. Sun, M. Liu, K. Li, Y. Zuo, Y. Han, J. Wang, C. Song, G. Zhang, X. Guo, Facile synthesis of Fe-containing metal–organic frameworks as highly efficient catalysts for degradation of phenol at neutral pH and ambient temperature, CrystEngComm, 17 (2015) 7160-7168.

[133] Y. Li, H. Liu, W.-J. Li, F.-Y. Zhao, W.-J. Ruan, A nanoscale Fe(II) metal–organic framework with a bipyridinedicarboxylate ligand as a high performance heterogeneous Fenton catalyst, RSC Adv. 6 (2016) 6756-6760.

[134] J. Tang, J. Wang, Iron-copper bimetallic metal-organic frameworks for efficient Fenton-like degradation of sulfamethoxazole under mild conditions, Chemosphere 241 (2020) 125002.

[135] P. Oancea, V. Meltzer, Photo-Fenton process for the degradation of Tartrazine (E102) in aqueous medium, J. Taiwan Inst. Chem. Eng. 44 (2013) 990-994.

[136] Y. Gao, G. Yu, K. Liu, S. Deng, B. Wang, J. Huang, Y. Wang, Integrated adsorption and visible-light photodegradation of aqueous clofibric acid and carbamazepine by a Fe-based metal-organic framework, Chem. Eng. J. 330 (2017) 157-165.

[137] R. Liang, S. Luo, F. Jing, L. Shen, N. Qin, L. Wu, A simple strategy for fabrication of Pd@MIL-100(Fe) nanocomposite as a visible-light-driven photocatalyst for the treatment of pharmaceuticals and personal care products (PPCPs), Appl. Catal. B 176-177 (2015) 240-248.

[138] R. Liang, R. Huang, S. Ying, X. Wang, G. Yan, L. Wu, Facile *in situ* growth of highly dispersed palladium on phosphotungstic-acid-encapsulated MIL-100(Fe) for the degradation of pharmaceuticals and personal care products

under visible light, Nano Res. 11 (2018) 1109-1123.

[139] J.-L. Qiu, J. Su, N. Muhammad, W.-T. Zheng, C.-L. Yue, F.-Q. Liu, J.-L. Zuo, Z.-J. Ding, Facile encapsulating Ag nanoparticles into a Tetrathiafulvalene-based Zr-MOF for enhanced Photocatalysis, Chem. Eng. J. 427 (2022) 131970.

[140] T.A. Vu, G.H. Le, C.D. Dao, L.Q. Dang, K.T. Nguyen, P.T. Dang, H.T.K. Tran, Q.T. Duong, T.V. Nguyen, G.D. Lee, Isomorphous substitution of Cr by Fe in MIL-101 framework and its application as a novel heterogeneous photo-Fenton catalyst for reactive dye degradation, RSC Adv. 4 (2014) 41185-41194.

[141] L. Qin, Z. Li, Z. Xu, X. Guo, G. Zhang, Organic-acid-directed assembly of iron–carbon oxides nanoparticles on coordinatively unsaturated metal sites of MIL-101 for green photochemical oxidation, Appl. Catal. B 179 (2015) 500-508.

[142] Z. Zhong, M. Li, J. Fu, Y. Wang, Y. Muhammad, S. Li, J. Wang, Z. Zhao, Z. Zhao, Construction of Cu-bridged $Cu_2O$/MIL(Fe/Cu) catalyst with enhanced interfacial contact for the synergistic photo-Fenton degradation of thiacloprid, Chem. Eng. J. 395 (2020) 125184.

[143] N. Liu, W. Huang, X. Zhang, L. Tang, L. Wang, Y. Wang, M. Wu, Ultrathin graphene oxide encapsulated in uniform MIL-88A(Fe) for enhanced visible light-driven photodegradation of RhB, Appl. Catal. B 221 (2018) 119-128.

[144] X. Li, Y. Pi, L. Wu, Q. Xia, J. Wu, Z. Li, J. Xiao, Facilitation of the visible light-induced Fenton-like excitation of $H_2O_2$ via heterojunction of g-$C_3N_4$/$NH_2$-Iron terephthalate metal-organic framework for MB degradation, Appl. Catal. B 202 (2017) 653-663.

[145] H. Zhao, Y. Chen, Q. Peng, Q. Wang, G. Zhao, Catalytic activity of MOF(2Fe/Co)/carbon aerogel for improving $H_2O_2$ and OH generation in solar photo–electro–Fenton process, Appl. Catal. B 203 (2017) 127-137.

[146] D.A. Armstrong, R.E. Huie, W.H. Koppenol, S.V. Lymar, G. Merényi, P. Neta, B. Ruscic, D.M. Stanbury, S. Steenken, P. Wardman, Standard electrode potentials involving radicals in aqueous solution: inorganic radicals (IUPAC Technical Report), 87 (2015) 1139.

[147] J. Wang, S. Wang, Activation of persulfate (PS) and peroxymonosulfate (PMS) and application for the degradation of emerging contaminants, Chem. Eng. J. 334 (2018) 1502-1517.

[148] P. Devi, U. Das, A.K. Dalai, In-situ chemical oxidation: Principle and applications of peroxide and persulfate treatments in wastewater systems, Sci. Total Environ. 571 (2016) 643-657.

[149] M. Siegert, J.M. Sonawane, C.I. Ezugwu, R. Prasad, Economic assessment of nanomaterials in bio-electrical water treatment, in: Prasad R., Karchiyappan T. (eds), Advanced Research in Nanosciences for Water Technology, Nanotechnology in the Life Sciences, Springer 2019, pp. 1-23.

[150] X. Li, W. Guo, Z. Liu, R. Wang, H. Liu, Quinone-modified $NH_2$-MIL-101(Fe) composite as a redox mediator for improved degradation of bisphenol A, J. Hazard. Mater. 324 (2017) 665-672.

[151] Y. Gao, S. Li, Y. Li, L. Yao, H. Zhang, Accelerated photocatalytic degradation of organic pollutant over metal-organic framework MIL-53 (Fe) under visible LED light mediated by persulfate, Appl. Catal. B 202 (2017) 165-174.

[152] X. Li, W. Guo, Z. Liu, R. Wang, H. Liu, Fe-based MOFs for efficient adsorption and degradation of acid orange 7 in aqueous solution via persulfate activation, Appl. Surf. Sci. 369 (2016) 130-136.

[153] J. Wang, J. Wan, Y. Ma, Y. Wang, M. Pu, Z. Guan, Metal–organic frameworks MIL-88A with suitable synthesis conditions and optimal dosage for effective catalytic degradation of Orange G through persulfate activation, RSC Advances 6 (2016) 112502-112511.

[154] M. Pu, Y. Ma, J. Wan, Y. Wang, J. Wang, M.L. Brusseau, Activation performance and mechanism of a novel heterogeneous persulfate catalyst: metal–organic framework MIL-53(Fe) with FeII/FeIII mixed-valence coordinatively unsaturated iron center, Catal. Sci. Technol 7 (2017) 1129-1140.

[155] M.-W. Zhang, M.-T. Yang, S. Tong, K.-Y.A. Lin, Ferrocene-modified iron-based metal-organic frameworks as an enhanced catalyst for activating oxone to degrade pollutants in water, Chemosphere 213 (2018) 295-304.

[156] S. Sajjadi, A. Khataee, N. Bagheri, M. Kobya, A. Şenocak, E. Demirbas, A.G. Karaoğlu, Degradation of diazinon pesticide using catalyzed persulfate with $Fe_3O_4$@MOF-2 nanocomposite under ultrasound irradiation, J. Ind. Eng. Chem. 77 (2019) 280-290.

[157] H. Chi, J. Wan, Y. Ma, Y. Wang, S. Ding, X. Li, Ferrous metal-organic frameworks with stronger coordinatively unsaturated metal sites for persulfate activation to effectively degrade dibutyl phthalate in wastewater, J. Hazard. Mater. 377 (2019) 163-171.

[158] M.R. Azhar, P. Vijay, M.O. Tadé, H. Sun, S. Wang, Submicron sized water-stable metal organic framework (bio-MOF-11) for catalytic degradation of pharmaceuticals and personal care products, Chemosphere 196 (2018) 105-114.

[159] W. Zhang, C. Yin, Y. Jin, X. Feng, X. Li, A. Xu, Co-MOF as a highly efficient catalyst for contaminants degradation via sulfite activation, Inorg. Chem. Commun. 126 (2021) 108498.

[160] A.J. Sisi, A. Khataee, M. Fathinia, B. Vahid, Ultrasonic-assisted degradation of a triarylmethane dye using combined peroxydisulfate and MOF-2 catalyst: Synergistic effect and role of oxidative species, J. Mol. Liq. 297 (2020) 111838.

[161] H. Li, J. Wan, Y. Ma, Y. Wang, X. Chen, Z. Guan, Degradation of refractory dibutyl phthalate by peroxymonosulfate activated with novel catalysts cobalt metal-organic frameworks: Mechanism, performance, and stability, J. Hazard. Mater. 318 (2016) 154-163.

[162] H. Li, J. Qin, Y. Zhang, S. Xu, J. Du, J. Tang, The efficiency and mechanism of dibutyl phthalate removal by copper-based metal organic frameworks coupled with persulfate, RSC Adv. 8 (2018) 39352-39361.

[163] T. Zeng, X. Zhang, S. Wang, H. Niu, Y. Cai, Spatial confinement of a $Co_3O_4$ catalyst in hollow metal–organic frameworks as a nanoreactor for improved degradation of organic pollutants, Environ. Sci. Technol. 49 (2015) 2350-2357.

[164] L. Nirumand, S. Farhadi, A. Zabardasti, A. Khataee, Synthesis and sonocatalytic performance of a ternary magnetic MIL-101(Cr)/RGO/$ZnFe_2O_4$ nanocomposite for degradation of dye pollutants, Ultrason. Sonochem. 42 (2018) 647-658.

[165] H. Li, Y. Yao, J. Chen, C. Wang, J. Huang, J. Du, S. Xu, J. Tang, H. Zhao, M. Huang, Heterogeneous activation of peroxymonosulfate by bimetallic MOFs for efficient degradation of phenanthrene: Synthesis, performance, kinetics, and mechanisms, Sep. Purif. Technol. 259 (2021) 118217.

[166] Z. Ye, J.A. Padilla, E. Xuriguera, E. Brillas, I. Sirés, Magnetic MIL(Fe)-type MOF-derived N-doped nano-ZVI@C rods as heterogeneous catalyst for the electro-Fenton degradation of gemfibrozil in a complex aqueous matrix, Appl. Catal. B 266 (2020) 118604.

[167] P. Liang, C. Zhang, X. Duan, H. Sun, S. Liu, M.O. Tade, S. Wang, An insight into metal organic framework derived N-doped graphene for the oxidative degradation of persistent contaminants: formation mechanism and generation of singlet oxygen from peroxymonosulfate, Environ. Sci. Nano 4 (2017) 315-324.

[168] S. Yang, X. Qiu, P. Jin, M. Dzakpasu, X.C. Wang, Q. Zhang, L. zhang, L. Yang, D. Ding, W. Wang, K. Wu, MOF-templated synthesis of $CoFe_2O_4$ nanocrystals and its coupling with peroxymonosulfate for degradation of bisphenol A, Chem. Eng. J. 353 (2018) 329-339.

[169] X. Li, Z. Ao, J. Liu, H. Sun, A.I. Rykov, J. Wang, Topotactic transformation of metal–organic frameworks to graphene-encapsulated transition-metal nitrides as efficient Fenton-like catalysts, ACS Nano 10 (2016) 11532-11540.

[170] Z. Li, X. Tang, G. Huang, X. Luo, D. He, Q. Peng, J. Huang, M. Ao, K. Liu, Bismuth MOFs based hierarchical $Co_3O_4$-$Bi_2O_3$ composite: An efficient heterogeneous peroxymonosulfate activator for azo dyes degradation, Sep. Purif. Technol. 242 (2020) 116825.

[171] W. Shao, C. He, M. Zhou, C. Yang, Y. Gao, S. Li, L. Ma, L. Qiu, C. Cheng, C. Zhao, Core–shell-structured MOF-derived 2D hierarchical nanocatalysts with enhanced Fenton-like activities, J. Mater. Chem. A 8 (2020) 3168-3179.

[172] J. Cao, S. Sun, X. Li, Z. Yang, W. Xiong, Y. Wu, M. Jia, Y. Zhou, C. Zhou, Y. Zhang, Efficient charge transfer in aluminum-cobalt layered double hydroxide derived from Co-ZIF for enhanced catalytic degradation of tetracycline through peroxymonosulfate activation, Chem. Eng. J. 382 (2020) 122802.

[173] X. Zhao, W. Wu, G. Jing, Z. Zhou, Activation of sulfite autoxidation with $CuFe_2O_4$ prepared by MOF-templated method for abatement of organic contaminants, Environ. Pollut. 260 (2020) 114038.

[174] Y. Li, H. Xu, S. Ouyang, J. Ye, Metal–organic frameworks for photocatalysis, Phys. Chem. Chem. Phys. 18 (2016) 7563-7572.

[175] Y. Pi, X. Li, Q. Xia, J. Wu, Y. Li, J. Xiao, Z. Li, Adsorptive and photocatalytic removal of Persistent Organic Pollutants (POPs) in water by metal-organic frameworks (MOFs), Chem. Eng. J. 337 (2018) 351-371.

[176] Q. Wang, Q. Gao, A.M. Al-Enizi, A. Nafady, S. Ma, Recent advances in MOF-based photocatalysis: environmental remediation under visible light, Inorg. Chem. Front. 7 (2020) 300-339.

[177] C.I. Ezugwu, S. Liu, C. Li, S. Zhuiykov, S. Roy, F. Verpoort, Engineering metal-organic frameworks for efficient photocatalytic conversion of $CO_2$ into solar fuels, Coord. Chem. Rev. 450 (2022) 214245.

[178] M. Alvaro, E. Carbonell, B. Ferrer, F.X. Llabrés i Xamena, H. Garcia, Semiconductor behavior of a metal-organic framework (MOF), Chem. Eur. J. 13 (2007) 5106-5112.

[179] X. Zhang, J. Wang, X.-X. Dong, Y.-K. Lv, Functionalized metal-organic frameworks for photocatalytic degradation of organic pollutants in environment, Chemosphere 242 (2020) 125144.

[180] K. Guesh, C.A.D. Caiuby, Á. Mayoral, M. Díaz-García, I. Díaz, M. Sanchez-Sanchez, Sustainable preparation of MIL-100(Fe) and its photocatalytic behavior in the degradation of Methyl Orange in water, Cryst. Growth Des. 17 (2017) 1806-1813.

[181] D. Wang, F. Jia, H. Wang, F. Chen, Y. Fang, W. Dong, G. Zeng, X. Li, Q. Yang, X. Yuan, Simultaneously efficient adsorption and photocatalytic degradation of tetracycline by Fe-based MOFs, J. Colloid Interface Sci. 519 (2018) 273-284.

[182] T. Araya, C.-c. Chen, M.-k. Jia, D. Johnson, R. Li, Y.-p. Huang, Selective degradation of organic dyes by a resin modified Fe-based metal-organic framework under visible light irradiation, Opt. Mater. 64 (2017) 512-523.

[183] C.-C. Wang, Y.-Q. Zhang, T. Zhu, P. Wang, S.-J. Gao, Photocatalytic degradation of methylene blue and methyl orange in a Zn(II)-based metal–organic framework, Desalin. Water Treat. 57 (2016) 17844-17851.

[184] W. Huang, C. Jing, X. Zhang, M. Tang, L. Tang, M. Wu, N. Liu, Integration of plasmonic effect into spindle-shaped MIL-88A(Fe): Steering charge flow for enhanced visible-light photocatalytic degradation of ibuprofen, Chem. Eng. J. 349 (2018) 603-612.

[185] C. Yang, X. You, J. Cheng, H. Zheng, Y. Chen, A novel visible-light-driven In-based MOF/graphene oxide composite photocatalyst with enhanced photocatalytic activity toward the degradation of amoxicillin, Appl. Catal. B 200 (2017) 673-680.

[186] J. Ding, Z. Yang, C. He, X. Tong, Y. Li, X. Niu, H. Zhang, UiO-66(Zr) coupled with $Bi_2MoO_6$ as photocatalyst for visible-light promoted dye degradation, J. Colloid Interface Sci. 497 (2017) 126-133.

[187] Z. Sha, J. Wu, Enhanced visible-light photocatalytic performance of BiOBr/UiO-66(Zr) composite for dye degradation with the assistance of UiO-66, RSC Adv. 5 (2015) 39592-39600.

[188] Z. Sha, J. Sun, H.S.O. Chan, S. Jaenicke, J. Wu, Enhanced photocatalytic activity of the AgI/UiO-66(Zr) composite for Rhodamine B degradation under visible-light irradiation, ChemPlusChem 80 (2015) 1321-1328.

[189] Y. Xue, P. Wang, C. Wang, Y. Ao, Efficient degradation of atrazine by BiOBr/UiO-66 composite photocatalyst under visible light irradiation: Environmental factors, mechanisms and degradation pathways, Chemosphere 203 (2018) 497-505.

[190] S. Gholizadeh Khasevani, M.R. Gholami, Evaluation of the reaction mechanism for

photocatalytic degradation of organic pollutants with MIL-88A/BiOI structure under visible light irradiation, Res. Chem. Intermed. 45 (2019) 1341-1356.

[191] Q. Hu, J. Di, B. Wang, M. Ji, Y. Chen, J. Xia, H. Li, Y. Zhao, In-situ preparation of $NH_2$-MIL-125(Ti)/BiOCl composite with accelerating charge carriers for boosting visible light photocatalytic activity, Appl. Surf. Sci. 466 (2019) 525-534.

[192] Z. Yang, J. Ding, J. Feng, C. He, Y. Li, X. Tong, X. Niu, H. Zhang, Preparation of $BiVO_4$/MIL-125(Ti) composite with enhanced visible-light photocatalytic activity for dye degradation, Appl. Organomet. Chem. 32 (2018) e4285.

[193] X. Zhao, Y. Zhou, Q. Liang, M. Zhou, Z. Li, S. Xu, Coupling MOF-derived titanium oxide with $CdIn_2S_4$ formed 2D/3D core-shell heterojunctions with enhanced photocatalytic performance, Sep. Purif. Technol. (2021) 119765.

[194] W. Guan, X. Gao, G. Ji, Y. Xing, C. Du, Z. Liu, Fabrication of a magnetic nanocomposite photocatalysts $Fe_3O_4$@ZIF-67 for degradation of dyes in water under visible light irradiation, J. Solid State Chem. 255 (2017) 150-156.

[195] H. Wang, X. Yuan, Y. Wu, G. Zeng, X. Chen, L. Leng, H. Li, Synthesis and applications of novel graphitic carbon nitride/metal-organic frameworks mesoporous photocatalyst for dyes removal, Appl. Catal. B 174-175 (2015) 445-454.

[196] J. Huang, X. Zhang, H. Song, C. Chen, F. Han, C. Wen, Protonated graphitic carbon nitride coated metal-organic frameworks with enhanced visible-light photocatalytic activity for contaminants degradation, Appl. Surf. Sci. 441 (2018) 85-98.

[197] Y. Zhang, J. Zhou, Q. Feng, X. Chen, Z. Hu, Visible light photocatalytic degradation of MB using UiO-66/g-$C_3N_4$ heterojunction nanocatalyst, Chemosphere 212 (2018) 523-532.

[198] H. Wang, X. Yuan, Y. Wu, G. Zeng, H. Dong, X. Chen, L. Leng, Z. Wu, L. Peng, *In situ* synthesis of $In_2S_3$@MIL-125(Ti) core–shell microparticle for the removal of tetracycline from wastewater by integrated adsorption and visible-light-driven photocatalysis, Appl. Catal. B 186 (2016) 19-29.

[199] W. Dong, D. Wang, H. Wang, M. Li, F. Chen, F. Jia, Q. Yang, X. Li, X. Yuan, J. Gong, H. Li, J. Ye, Facile synthesis of $In_2S_3$/UiO-66 composite with enhanced adsorption performance and photocatalytic activity for the removal of tetracycline under visible light irradiation, J. Colloid Interface Sci. 535 (2019) 444-457.

[200] A.A. Oladipo, R. Vaziri, M.A. Abureesh, Highly robust $AgIO_3$/MIL-53(Fe) nanohybrid composites for degradation of organophosphorus pesticides in single and binary systems: Application of artificial neural networks modelling, J. Taiwan Inst. Chem. Eng. 83 (2018) 133-142.

[201] S.-W. Lv, J.-M. Liu, N. Zhao, C.-Y. Li, Z.-H. Wang, S. Wang, A novel cobalt doped MOF-based photocatalyst with great applicability as an efficient mediator of peroxydisulfate activation for enhanced degradation of organic pollutants, New J. Chem. 44 (2020) 1245-1252.

[202] Y. Zhang, J. Zhou, X. Chen, L. Wang, W. Cai, Coupling of heterogeneous advanced oxidation processes and photocatalysis in efficient degradation of tetracycline hydrochloride by Fe-based MOFs: Synergistic effect and degradation pathway, Chem. Eng. J. 369 (2019) 745-757.

[203] M. Zhong, S.-Y. Qu, K. Zhao, P. Fei, M.-M. Wei, H. Yang, B. Su, Bimetallic metal-organic framework derived ZnO/$Ni_{0.9}Zn_{0.1}O$ nanocomposites for improved photocatalytic degradation of organic dyes, ChemistrySelect 5 (2020) 1858-1864.